Inelastic excitations and momentum distributions in kinematically complete breakup reactions of two-neutron halo nuclei

S. N. Ershov,* B. V. Danilin,† and J. S. Vaagen
SENTEF, Department of Physics, University of Bergen, Bergen, Norway
(Received 29 January 2001; published 20 November 2001)

A microscopic quantum-mechanical approach to breakup reactions into the low-energy continuum of Borromean two-neutron halo nuclei is developed, taking simultaneously into account Coulomb and nuclear dissociation. The importance of including both elastic and inelastic fragmentation is demonstrated for ^{6}He breakup on C and Pb targets at intermediate energies, for kinematically complete experiments. Recent GSI experimental data are analyzed quantitatively and the results reveal a rich and complex interplay of reaction mechanisms and low-lying halo excitations.

DOI: 10.1103/PhysRevC.64.064609 PACS number(s): 21.45.+v, 21.60.Gx, 24.30.Gd, 27.20.+n

I. INTRODUCTION

The discovery of halo structure in light nuclei at the neutron dripline has given new impetus to theoretical investigations of nuclear structure and reaction mechanisms. In a new generation of kinematically complete experiments, unique data on halo excitation functions are becoming accessible, revealing the continuum spectrum as well as different correlations between halo fragments. This demands developing microscopic models that properly take into account the degrees of freedom and dynamics responsible for halo structure. Thus current emphasis is on understanding the intrinsic properties of both bound and excited states that are intertwined by reaction mechanisms and expressed through inclusive or exclusive observables that often are also distorted by detection efficiency and finite acceptance of experimental installations.

The characteristic features of halo phenomena are connected not only with the specific structure of the ground-state wave function (weak binding, spatial granularity, and large extension) but also with excitation of halo degrees of freedom, reflected in the structure of the low-lying continuum which, near the three-body breakup threshold, reveals accumulation of the transition strength for different multipole excitations, the so-called soft modes.

Highly integrated observables, measured in a variety of reactions, show different sensitivity to the presence of halo structure. The halo increases the reaction cross section and the scale of the effect is a few tenths. The width of fragment momentum distributions becomes a few times narrower, while the electromagnetic dissociation cross sections are increased by orders of magnitude compared to reactions with stable nuclei [1]. The sensitivity is defined by the role that the transitions from the ground state to the low-energy continuum play in the reaction, and is increased to a maximum for Coulomb dissociation. When excited to the low-lying continuum, the halo nucleus subsequently breaks up into the heavy core and halo nucleons. The core detection in a fragmentation reaction primarily selects a peripheral collision, but may correspond to a wide spectrum of excitation energies in the halo nucleus. A simultaneous detection of all fragments allows reconstruction of the halo spectrum and singles out the low energy part, thus underlining the reaction mechanism that is the most sensitive to the halo structure. In addition, a variety of angular and energy correlations of detected fragments become accessible and shed light on intimate details of interaction dynamics of exotic nuclei.

Different reaction mechanisms such as Coulomb or nuclear dissociation may emphasize different sides of these correlations. To quantitatively understand them, the Coulomb and nuclear interactions have to be treated on equal footing, explicitly taking into account the Coulomb-nuclear interference.

There are different approaches to breakup dynamics in reactions with unstable nuclei. A simple and extensively used model for energetic fragmentation is the Serber model [2], based on the sudden approximation, but which only includes ground-state correlations. This procedure has to be improved to make the extracted information on nuclear structure more quantitatively meaningful. The interactions with the target should be included at a dynamical level, and correlations caused by final-state interactions (FSI) between outgoing halo fragments should be considered. In applications to halo physics several attempts exist [3–9] that deal in different ways with these questions, but a consistent microscopic treatment for the case of two-neutron halo nuclei has not been developed yet. At *low halo excitation* energies, when relative velocities of halo fragments are small, it is necessary to take into account all final-state interactions, and the spectator model (knockout of constituents in halo nuclei) and, in particular, the no-FSI approximation are invalid. This has motivated us to develop a reaction model where the complex nature of the low-energy continuum is treated in an accurate way. To test the model, reactions with ^{6}He were considered.

The ^{6}He nucleus has become, both theoretically and experimentally, the test bench for a series of Borromean halo nuclei such as ^{11}Li, ^{14}Be, etc. Recently, a variety of theoretical methods and models have also been developed for the resonance structure of halo excitations. For the continuum structure, a striking observation has been made. While the

*Permanent address: JINR, RU-141980 Dubna, Russia.
†Permanent address: RRC The Kurchatov Institute, RU-123182 Moscow, Russia.

well-known three-body 2^+ resonance in ^{6}He is reproduced, all three-body calculations [10,11] have given a peaking of the strength concentration for the soft dipole mode at 1.2 MeV from the three-body threshold, which is not observed in recent experiments with ^{6}He [12]. This has called for further investigation within the cluster three-body dynamics.

To fully understand the detailed Borromean halo excitation structure of a nucleus such as ^{6}He, at least a four-body reaction theory is necessary. A full-scale four-body theory that takes into account available reaction channels and the complex structure of the constituents, has not been formulated. But for definite physical conditions, simplification of the reaction mechanism makes it possible to develop a viable approach. At intermediate energies the one-step reaction mechanism dominates and the Glauber or distorted wave impulse approximation (DWIA) can be applied. These approaches contain as a main part the microscopic three-body structure of the ground state (Glauber elastic scattering [13]), and also final discrete states in DWIA charge-exchange reactions [14], and the exact three-body continuum [15]. The latter enables us to study, in principle, the internal halo structure via all possible fragment correlations.

Recently [16], in diffractive breakup of Borromean halo nuclei on *proton* target, we demonstrated the crucial role of the correlated continuum excitations in the fragment momentum distribution, within a microscopic four-body DWIA theory. We have now extended this approach to breakup reactions on *nuclear* targets, especially suitable for a complete kinematic experiment, which gives information about all beam and fragment momenta (except the recoil of the target nucleus). Such experiments allow sophisticated analysis of the data and give a possibility to reconstruct projectile excitation spectra and different correlations between fragments. But still some ambiguity exists since the energy transferred to the target can be distributed in different ways between internal excitations and center-of-mass motion.

To be compared with experimental data that include excited final target states, the theoretical models have to take into account the presence of different reaction mechanisms leading to elastic and inelastic fragmentations, i.e., when the target remains in the ground state or goes to excited states, respectively. Recently, a short report on our approach was presented [17]. Now, a detailed study of inelastic halo excitations, different energy and angular correlations, longitudinal and transverse momentum distributions for elastic and inelastic ^{6}He breakup reactions on ^{12}C (light target, nuclear interaction dominates) and ^{208}Pb (heavy target, Coulomb dissociation is the main process) will be described and compared with recent experimental data from GSI [12,18–20] at collision energy 240 MeV/nucleon. The recoil of all halo constituents [15] is now fully included. The material contained in this paper is organized as follows. Section II describes the formalism in details. The discussion of results and comparison of calculations with experimental data are given in Sec. III. Finally, Sec. IV contains the main conclusions of this work.

II. REACTION FORMALISM

The cross section of the breakup reaction $a+A\to n_1+n_2+n_3+A'$, involving collision of projectile a (two-neutron halo nucleus that breaks up into three fragments n_i) and target nucleus A, can be written in the following way:

$$\sigma=\frac{(2\pi)^4}{\hbar v_i}\sum_{A'}\int d\boldsymbol{k}_1 d\boldsymbol{k}_2 d\boldsymbol{k}_3 d\boldsymbol{k}_{A'}\,\delta(E_f-E_i)\times\delta(\boldsymbol{P}_f-\boldsymbol{P}_i)|T_{fi}|^2, \tag{1}$$

where summation is over target excited states A' (0 labels the ground state). Here $E_i=\varepsilon_a+\varepsilon_A$, $E_f=\varepsilon_1+\varepsilon_2+\varepsilon_3+\varepsilon_{A'}+E_{A'}+Q$, $\boldsymbol{P}_i=\boldsymbol{k}_a+\boldsymbol{k}_A$, $\boldsymbol{P}_f=\boldsymbol{k}_1+\boldsymbol{k}_2+\boldsymbol{k}_3+\boldsymbol{k}_{A'}$ are the total energies and momenta of all particles before and after collisions. Q is the separation energy of the halo nucleus, while $E_{A'}$ ($=0$, for ground state) is the excitation energy of the target in state A', ε_j is a kinetic energy of particle j. The relative incident velocity is $v_i=\hbar k_i/\mu_i$, and $\mu_i=m_aM_A/(m_a+M_A)$ is the reduced mass of the particles before collision with $m_a=m_1+m_2+m_3$. We use the $(a+A)$ center-of-mass (c.m.) coordinate frame ($\boldsymbol{P}_i=0,\boldsymbol{k}_A=-\boldsymbol{k}_a=\boldsymbol{k}_i,E_i=\varepsilon_i=\hbar^2k_i^2/2\mu_i$). The Jacobi coordinates for particles both in initial and final systems are given by

$$\boldsymbol{k}_x=\mu_x\left(\frac{\boldsymbol{k}_2}{m_2}-\frac{\boldsymbol{k}_1}{m_1}\right),\quad \mu_x=\frac{m_1m_2}{m_1+m_2},$$

$$\boldsymbol{k}_y=\mu_y\left(\frac{\boldsymbol{k}_3}{m_3}-\frac{\boldsymbol{k}_1+\boldsymbol{k}_2}{m_1+m_2}\right),\quad \mu_y=\frac{(m_1+m_2)m_3}{m_1+m_2+m_3},$$

$$\boldsymbol{k}_f=\mu_f\left(\frac{\boldsymbol{k}_{A'}}{m_A}-\frac{\boldsymbol{k}_1+\boldsymbol{k}_2+\boldsymbol{k}_3}{m_a}\right),\quad \mu_f=\frac{m_aM_A}{m_a+M_A},$$

$$\boldsymbol{P}_f=0,\quad \boldsymbol{k}_1+\boldsymbol{k}_2+\boldsymbol{k}_3=-\boldsymbol{k}_{A'}=-\boldsymbol{k}_f. \tag{2}$$

Jacobi vectors $(\boldsymbol{k}_x,\boldsymbol{k}_y)$ characterize the relative motion of the three projectile-breakup fragments, and $\boldsymbol{k}_f$ the relative target-projectile c.m. motion. In the c.m. frame $E_f=\varepsilon_f+E_\kappa+Q+E_{A'}$, where $\varepsilon_f=\hbar^2k_f^2/2\mu_f$ is the kinetic energy of relative $(n_1+n_2+n_3)+A$ motion in the exit channel, while $E_\kappa=\varepsilon_x+\varepsilon_y=\hbar^2k_x^2/2\mu_x+\hbar^2k_y^2/2\mu_y$ is the internal projectile excitation energy measured from the breakup threshold and consisting of kinetic energies of projectile fragments in a system where the projectile is at rest.[1] The corresponding coordinate system in configuration space is shown in Fig. 1 and is discussed in details in Sec. II F.

The matrix element T_{fi} in Eq. (1) includes all interaction dynamics and is given in prior representation by

$$T_{fi}=\langle\Psi_{A'}^{(-)}(\boldsymbol{k}_x,\boldsymbol{k}_y,\boldsymbol{k}_f),\Phi_{A'}|\times\sum_{p,t}V_{pt}-U_{aA}|\Psi_0,\Phi_0,\chi_0^{(+)}(\boldsymbol{k}_i)\rangle, \tag{3}$$

[1]Notice a few notational changes when compared with [15], such as $C\to3$, $A\to a$, $N\to A$, and that a misprint of the sign of $\boldsymbol{k}_x$ has been corrected.

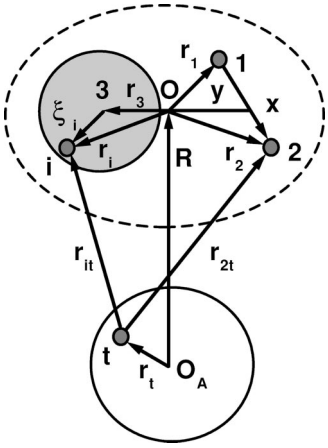

FIG. 1. Spatial coordinates in the nucleus-nucleus collision.

where Ψ_0 is the halo ground-state wave function while $\Psi^{(-)}_{A'}(\boldsymbol{k}_x,\boldsymbol{k}_y,\boldsymbol{k}_f)$ is the exact continuum wave function that describes relative motion of the halo fragments n_i and the target in an excited state $\Phi_{A'}$. To get $\Psi^{(-)}_{A'}$ one has to solve equations of the Faddeev-Yakubovsky type, taking into account the complex nature of the constituents. An exact solution has not been feasible up to now and approximate methods are required. We make approximations at the level of the reaction mechanism but treat the three-body structure of the halo projectile in a consistent way keeping the characteristics of the halo structure. They are contained directly in the halo ground-state wave function Ψ_0 and in the low-lying excitation spectra where strength concentration of transitions with different multipolarities are formed. If there is no direct knockout of a projectile constituent we cannot neglect any of its mutual interactions. All projectile fragments take similar part in the interaction process. This is realized for the soft part of a halo spectrum where relative fragment velocities are small and restricted kinematically by the low excitation energy E_κ. At low E_κ there are *no spectator* particles. Hence, we factorize $\Psi^{(-)}_{A'}(\boldsymbol{k}_x,\boldsymbol{k}_y,\boldsymbol{k}_f)$ explicitly extracting a wave function of the excited projectile

$$\langle \Psi^{(-)}_{A'}(\boldsymbol{k}_x,\boldsymbol{k}_y,\boldsymbol{k}_f)| \simeq \langle \chi^{(-)}_{A'}(\boldsymbol{k}_f), \Psi^{(-)}(\boldsymbol{k}_x,\boldsymbol{k}_y)|, \qquad (4)$$

where $\Psi^{(-)}(\boldsymbol{k}_x,\boldsymbol{k}_y)$ is a continuum three-body wave function of the halo system with excitation energy E_κ. $\chi^{(-)}_{A'}(\boldsymbol{k}_f)$ is a distorted wave describing relative motion of projectile and target in excited state A' and depends on the relative coordinate $\boldsymbol{R}$ between the ejectile c.m.$_a$ and the target c.m.$_A$. Such distorted waves $\chi^{(-)}_{A'}(\boldsymbol{k}_f)$ can be used if the reaction is fast and the loss of energy is small compared with the initial collision energy. This is different from the case where a constituent due to nuclear interaction with the target, is kicked out of the halo nucleus, and its relative velocity is significant in comparison with the rest of the halo system, what corresponds to high excitation energy E_κ. Then the interactions between ''participant'' (kicked out fragment) and ''spectators'' (the two others halo constituents) can be neglected in describing the state of the ejectile. Under such conditions a ''spectator'' approach is justified and a factorization of $\Psi^{(-)}_{A'}(\boldsymbol{k}_x,\boldsymbol{k}_y,\boldsymbol{k}_f)$ other than that in Eq. (4) has to be used.

Within approximation (4) the reaction amplitude can be written as

$$T_{fi} = \langle \chi^{(-)}_{A'}(\boldsymbol{k}_f), \Phi_{A'}, \Psi^{(-)}(\boldsymbol{k}_x,\boldsymbol{k}_y)| \times \sum_{p,t} V_{pt} |\Psi_0, \Phi_0, \chi^{(+)}_0(\boldsymbol{k}_i)\rangle. \qquad (5)$$

The optical potential U_{aA} depends on the c.m. distance between a and A and defines the distorted wave χ^+_0 describing the relative motion of the colliding nuclei in the initial channel. $\Sigma_{p,t}V_{pt}$ is composed of effective nucleon-nucleon interactions V_{pt} between projectile (p) and target (t) nucleons and governs the fragmentation process in the breakup reactions. The optical potential U_{aA} does not give contribution to Eq. (5) due to orthogonality between the bound Ψ_0 and excited $\Psi^{(-)}(\boldsymbol{k}_x,\boldsymbol{k}_y)$ states of the halo projectile. The post and prior forms of the breakup amplitude T_{fi} are equal in our approximation since the decomposition of the Hamiltonian into perturbed and unperturbed parts is the same for initial and final channels. According to this expression *the breakup is treated as an inelastic excitation of the halo projectile directly to the continuum* $\Psi^{(-)}(\boldsymbol{k}_x,\boldsymbol{k}_y)$. Whether this continuum state will be resonant or nonresonant depends on the final state interactions between the fragments.

A. Separation into elastic and inelastic breakup

The inclusive cross section (1) includes elastic and inelastic breakup. By elastic (inelastic) breakup we mean breakup of the halo projectile in an encounter leaving the target in ground (excited) state. In order to single out their contributions separately we use the method of Refs. [21–23], where the energy δ function is expressed by the imaginary part of energy denominator, which is subsequently replaced by the many-body Green's function. Thus we can write

$$\sum_{A'} \int d\boldsymbol{k}_f \delta(\omega - \varepsilon_f - E_{A'}) |\langle \chi^{(-)}_{A'}(\boldsymbol{k}_f), \Phi_{A'}|V_{aA}|\Phi_0\rangle|^2 = \sum_{A'} \int d\boldsymbol{k}_f \left(-\frac{1}{\pi}\right) \mathrm{Im} \frac{\langle \Phi_0|V_{aA}|\Phi_{A'}, \chi^{(-)}_{A'}(\boldsymbol{k}_f)\rangle \langle \chi^{(-)}_{A'}(\boldsymbol{k}_f), \Phi_{A'}|V_{aA}|\Phi_0\rangle}{\omega - \varepsilon_f - E_{A'} + \imath\eta}$$
$$= \left(-\frac{1}{\pi}\right) \langle \Phi_0|V_{aA}\mathrm{Im}\mathcal{G}(\omega)V_{aA}|\Phi_0\rangle, \qquad (6)$$

where

$$\omega = \varepsilon_i - E_\kappa - Q$$

and

$$V_{aA} = \Psi^{(-)}(\boldsymbol{k}_x, \boldsymbol{k}_y) \Sigma_{p,t} V_{pt} \Psi_0 \chi_0^{(+)}(\boldsymbol{k}_i).$$

The many-body Green's function $\mathcal{G}(\omega)$ has following spectral representation:

$$\mathcal{G}(\omega) = \frac{1}{\omega - H_A - T_f - \tilde{U}_{aA} + \imath\eta} = \sum_{A'} \int d\boldsymbol{k}_f \frac{|\Phi_{A'} \chi_{A'}^{(-)}(\boldsymbol{k}_f)\rangle\langle\chi_{A'}^{(-)}(\boldsymbol{k}_f)\Phi_{A'}|}{\omega - \varepsilon_f - E_{A'} + \imath\eta}. \quad (7)$$

The H_A is the Hamiltonian of the target nucleus, $(E_{A'} - H_A)\Phi_{A'} = 0$. The distorted waves $\chi_{A'}^{(-)}(\boldsymbol{k}_f)$ are defined by the kinetic energy operator T_f and the optical potential $\tilde{U}_{aA}$, $(\varepsilon_f - T_f - \tilde{U}_{aA})\chi_{A'}^{(-)}(\boldsymbol{k}_f) = 0$. A practical way to deal with $\mathcal{G}(\omega)$ is to integrate out the internal coordinates by averaging over the target ground-state wave function Φ_0. The Φ_0 cannot be passed directly through matrix element (6) to the Green's function, since the NN interaction V_{pt} depends on internal target coordinates. Hence, we approximate $\mathrm{Im}\mathcal{G}(\omega)$ by its ground state expectation value [22,24] using the Green's function optical reduction

$$G(\omega) = \langle\Phi_0|\mathcal{G}(\omega)|\Phi_0\rangle = \frac{1}{\omega - T_f - \tilde{U}_{aA} + \imath\eta}. \quad (8)$$

The imaginary part of the Green's function satisfies the unitary identity [23]

$$\mathrm{Im}G(\omega) = (-\pi) \int d\boldsymbol{k} |\chi_0^{(-)}(\boldsymbol{k})\rangle \delta(\omega - \varepsilon_k) \langle\chi_0^{(-)}(\boldsymbol{k})| + G^+(\omega)\mathrm{Im}\tilde{U}_{aA} G(\omega). \quad (9)$$

Applying identity (9) in Eq. (6) one gets two terms that give a separation between elastic breakup with target in its ground state and inelastic breakup, which includes all possible transitions out of Φ_0. Thus, the inclusive cross section is decomposed into elastic σ_{el} and inelastic σ_{in} parts as $\sigma = \sigma_{el} + \sigma_{in}$, where

$$\sigma_{el} = \frac{(2\pi)^4}{\hbar v_i} \int d\boldsymbol{k}_x d\boldsymbol{k}_y d\boldsymbol{k}_f \delta(\varepsilon_i - \varepsilon_f - E_\kappa - Q) \times |\langle\chi_0^{(-)}(\boldsymbol{k}_f), \Phi_0, \Psi^{(-)}(\boldsymbol{k}_x, \boldsymbol{k}_y)| \times \sum_{p,t} V_{pt} |\Psi_0, \Phi_0, \chi_0^{(+)}(\boldsymbol{k}_i)\rangle|^2, \quad (10)$$

$$\sigma_{in} = \frac{(2\pi)^4}{\hbar v_i} \int d\boldsymbol{k}_x d\boldsymbol{k}_y \int d\boldsymbol{R} \frac{1}{\pi} [-\mathrm{Im}\tilde{U}_{aA}(\boldsymbol{R})] \times |\langle G(\boldsymbol{R}, \omega), \Phi_0, \Psi^{(-)}(\boldsymbol{k}_x, \boldsymbol{k}_y)| \times \sum_{p,t} V_{pt} |\Psi_0, \Phi_0, \chi_0^{(+)}(\boldsymbol{k}_i)\rangle|^2. \quad (11)$$

These expressions are the starting point for calculations of various cross sections, angular and energy correlations both for elastic and inelastic breakup. We notice that the expressions for σ_{el} and σ_{in} have similar structure. In Eq. (11) the integration over the radial dependence of the optical potential and Green's function is shown explicitly. In the matrix element for inelastic fragmentation, the optical model Green's function $G(\boldsymbol{R}, \omega)$ appears instead of the distorted wave $\chi_0^{(-)}(\boldsymbol{k}_f)$ in the elastic amplitude and an integration over the $\boldsymbol{R}$ coordinate weighted with the imaginary part of optical potential $\mathrm{Im}\tilde{U}_{aA}(\boldsymbol{R})$ replaces the integration over the direction of the momentum $\hat{\boldsymbol{k}}_f$. Therefore, in the approach we have developed, we can study the space localization of inelastic breakup processes, but the differential cross section for inelastic scattering of the halo nucleus can be calculated only for elastic fragmentation $d^3\sigma_{el}/d\hat{\boldsymbol{k}}_f dE_\kappa$, since the angular variables $\hat{\boldsymbol{k}}_f$ are not present in expression (11) for inelastic breakup.

B. Elastic breakup

The exclusive elastic breakup cross section (10) (when energies and momenta of all particles are observed), averaged over initial and summed over final spin projections, can be written as

$$\frac{d^8\sigma_{el}}{d\hat{\boldsymbol{k}}_f d\hat{\boldsymbol{k}}_x d\hat{\boldsymbol{k}}_y d\varepsilon_y dE_\kappa} = (2\pi)^4 \frac{\mu_i \mu_f}{\hbar^4} \frac{k_f}{k_i} 2\left(\frac{\mu_x \mu_y}{\hbar^4}\right)^{3/2} \times \frac{\sqrt{\varepsilon_y(E_\kappa - \varepsilon_y)}}{\hat{J}_i^2 \hat{J}_A^2} \sum_{M_{A'}, m_1, m_2, M_A, M_i} |T_{el}|^2, \quad (12)$$

where $\hat{J} = \sqrt{2J+1}$. The reaction amplitude T_{el} is given in the DW framework by

$$T_{el} = \langle\chi^{(-)}(\boldsymbol{k}_f), \Phi_{J_A M_{A'}}, \Psi_{m_1, m_2}^{(-)}(\boldsymbol{k}_x, \boldsymbol{k}_y)| \times \sum_{p,t} V_{pt} |\Psi_{J_i M_i}, \Phi_{J_A M_A}, \chi^{(+)}(\boldsymbol{k}_i)\rangle. \quad (13)$$

In Eq. (13) the wave-function dependence on the quantum numbers of angular momenta is shown explicitly. Here J_i and M_i (J_A and M_A) are the spin and spin projection of the projectile (target) ground state, m_1 and m_2 are the spin projections of halo neutrons after breakup. Since we are focusing on a study of ^{6}He, where one of the fragments is an α

particle with zero spin, we have omitted everywhere mentioning the core spin. For the nucleus-nucleus scattering addressed later, there is no spin dependence in optical potentials and the distorted waves $\chi^{(\pm)}$ do not depend on spin projections. The formulas below are presented explicitly for that case. When the target is a proton or a nucleus with nonzero spin, the optical potential has usually spin-orbit coupling and, the distorted waves depend on M_A. Generalization to such cases is straightforward but is not given here.

To calculate Eq. (13), the bound $\Psi_{J_i M_i}$ and continuum $\Psi^{(-)}_{m_1,m_2}(\boldsymbol{k}_x,\boldsymbol{k}_y)$ halo wave functions have to be generated by a nuclear model. For Borromean two-neutron halo nuclei, an understanding of the essential halo structure has been obtained in the framework of a three-body model [25]. In this model, the total wave function of ^{6}He is represented by a product of wave functions describing the internal structure of the α core and the relative motion of three interacting constituents, core and halo neutrons. The method of hyperspherical harmonics [26,27] has been used to treat the three-body interaction dynamics for both bound and scattering states and has given [14–16,28] a comprehensive description of data on weak and electromagnetic characteristics, (p,p') inelastic scattering and charge-exchange $(p,n),(n,p)$ reactions to bound and continuum states for $A=6$ systems. It is important to underline that in calculating the continuum wave functions $\Psi^{(-)}_{m_1,m_2}(\boldsymbol{k}_x,\boldsymbol{k}_y)$ the final state interaction (the pair interactions between all ejectile constituents) was fully taken into account. The same model for the halo wave functions is used in our calculations of the reaction amplitude (13).

In the method of hyperspherical harmonics the wave function above the breakup threshold is written as follows:

$$\Psi^{(+)}_{m_1,m_2}=\sum_{\delta,M_f,M_{L_f}}(s_1m_1s_2m_2|S_fM_{S_f})(L_fM_{L_f}S_fM_{S_f}|J_fM_f)\times\imath^{-K_f}\psi^{l_xl_y}_{K_f}(\alpha_\kappa)[Y_{l_x}(\hat{\boldsymbol{k}}_x)\otimes Y_{l_y}(\hat{\boldsymbol{k}}_y)]^*_{L_fM_{L_f}}\Psi_{\gamma J_fM_f}(\xi,\boldsymbol{x},\boldsymbol{y},\kappa), \tag{14}$$

where $\delta=\{J_f,\gamma\}=\{J_f,K_f,L_f,S_f,l_x,l_y\}$ is an abbreviation for a set of quantum numbers, which characterizes the relative motion of the three constituents flying apart in ^{6}He. The notation $[\cdots]$ indicates tensor coupling. The $\psi^{l_xl_y}_{K_f}(\alpha_\kappa)$ is the hyperangular part of the hyperharmonic

$$\psi^{l_xl_y}_{K_f}(\alpha_\kappa)=N^{l_xl_y}_{K_f}(\sin\alpha_\kappa)^{l_x}(\cos\alpha_\kappa)^{l_y}P^{l_x+1/2,l_y+1/2}_{(K_f-l_x-l_y)/2}(\cos2\alpha_\kappa), \tag{15}$$

where $P^{\alpha,\beta}_n$ are Jacobi polynomials and $N^{l_xl_y}_K$ is a normalization factor. The hyperangle α_κ is defined as $\cos^2\alpha_\kappa=\varepsilon_y/E_\kappa$. The continuum wave function $\Psi_{\gamma J_fM_f}(\xi,\boldsymbol{x},\boldsymbol{y},\kappa)$ depends on the quantum numbers γ, nuclear excitation energy E_κ (expressed by the hypermomentum $\kappa=\sqrt{2mE_\kappa/\hbar^2}$ with m being the nucleon mass), the internal α-particle coordinates ξ and Jacobian space coordinates $(\boldsymbol{x},\boldsymbol{y})$ (shown on Fig. 1), the total angular momentum J_f and its projections M_f,

$$\Psi_{\gamma J_fM_f}(\xi,\boldsymbol{x},\boldsymbol{y},\kappa)=\frac{\phi(\xi)}{(\kappa\rho)^{5/2}}\sum_{\gamma'}\chi_{\gamma\gamma'}(\kappa\rho)\psi^{l'_xl'_y}_{K'}(\alpha)\times\{[Y_{l'_x}(\hat{\boldsymbol{x}})\otimes Y_{l'_y}(\hat{\boldsymbol{y}})]_{L'}\otimes\chi_{S'}\}_{J_fM_f}\chi_{TM_T},$$

$$\tan\alpha=\frac{x}{y},\quad \rho=\sqrt{x^2+y^2}. \tag{16}$$

The $\phi(\xi)$ is the α-particle core wave function, $\chi_{S(T)}$ is a spin or isospin function. The hyper-radial wave function $\chi_{\gamma\gamma'}(\kappa\rho)$ is a solution of a set of coupled K-harmonic equations. The necessary details on how to solve a system of K-harmonic equations, choosing nucleon-nucleon and nucleon-core potentials in calculations of the three-body bound and continuum wave functions for ^{6}He, can be found in Ref. [10]. According to Eq. (14), the transition amplitude T_{el} can be further decomposed as

$$T_{el}=\sum_{\delta,M_{L_f},M_{S_f}}(s_1m_1s_2m_2|S_fM_{S_f})(L_fM_{L_f}S_fM_{S_f}|J_fM_f)\times\imath^{-K_f}\psi^{l_xl_y}_{K_f}(\alpha_\kappa)[Y_{l_x}(\hat{\boldsymbol{k}}_x)\otimes Y_{l_y}(\hat{\boldsymbol{k}}_y)]^*_{L_fM_{L_f}}T_\delta(\boldsymbol{k}_f,\boldsymbol{k}_i,\kappa). \tag{17}$$

The $T_\delta(\boldsymbol{k}_f,\boldsymbol{k}_i,\kappa)$ has now formally the same structure as any two-body amplitude for excitation of a nuclear state with total momentum J_f,M_f, excitation energy E_κ, and a fixed state of relative motion of breakup fragments defined by the quantum numbers γ,

$$T_\delta(\boldsymbol{k}_f,\boldsymbol{k}_i,\kappa)=\langle\chi^{(-)}(\boldsymbol{k}_f),\Phi_{J_AM_{A'}},\Psi_{\gamma J_fM_f}(\kappa)\times|\sum_{p,t}V_{pt}|\Psi_{J_iM_i},\Phi_{J_AM_A},\chi^{(+)}(\boldsymbol{k}_i)\rangle. \tag{18}$$

The effective NN interaction V_{pt} (assuming local interactions) depends on distance $\boldsymbol{r}_{pt}=\boldsymbol{r}_p-\boldsymbol{r}_t+\boldsymbol{R}$ between projectile (p) and target (t) nucleons (see Fig. 1), where $\boldsymbol{r}_{p,t}$ are nucleon coordinates relative to the c.m.$_{a,A}$, respectively, while $\boldsymbol{R}$ is the c.m. distance between target and projectile. Integrating over projectile $\boldsymbol{r}_p$ and target $\boldsymbol{r}_t$ internal coordinates, the nuclear form factors as a function of $\boldsymbol{R}$ can be defined as

$$\langle\Phi_{J_AM_{A'}},\Psi_{\gamma J_fM_f}|\sum_{p,t}V_{pt}|\Psi_{J_iM_i},\Phi_{J_AM_A}\rangle=\sum_{lj_pj_t}(J_iM_ij_pm_p|J_fM_f)(lm_lj_tm_t|j_pm_p)\times(J_AM_{A'}j_tm_t|J_AM_A)\imath^{-l}Y^*_{lm_l}(\hat{\boldsymbol{R}})F^\delta_{lj_tj_p}(R,\kappa), \tag{19}$$

where l, j_p, and j_t are the orbital, the total projectile, and target angular-momentum transfers, respectively. A convenient way to handle the complicated radial dependence in Eq. (19) is to perform the calculation of the radial form fac-

tor $F^{\delta}_{lj_tj_p}(R,\kappa)$ in momentum space [15,29,30], where the integrations over different space coordinates are reduced to a product of integrand factors. Using a Fourier-Bessel transformation

$$V_{pt}\equiv V(\boldsymbol{r}_{pt})=\frac{1}{(2\pi)^3}\int d\boldsymbol{k}V(\boldsymbol{k})\exp\{-\imath(\boldsymbol{r}_p-\boldsymbol{r}_t+\boldsymbol{R})\cdot\boldsymbol{k}\}, \tag{20}$$

a common decomposition of the effective nucleon-nucleon forces V_{pt} into operators acting on separate coordinates can be obtained [30]. Here we are presenting the calculations for a reaction on a target with zero spin $J_A=0$. In this case, if we neglect the two-body *NN* spin-orbital interaction (the usual approximation in nucleus-nucleus collisions), then only nonspinflip excitations of natural parity in the projectile are allowed [29] and only the central part of nucleon-nucleon forces can excite them. The formulas for radial form factors are given below for this case. Generalization to a more general situation is straightforward. After transition into momentum space, the radial part $F^{\delta}_{j_p0j_p}(R,\kappa)$ of the nuclear form factor can be written as

$$F^{\delta}_{j_p0j_p}(R,\kappa)=\int_0^\infty dkk^2j_l(kR)\imath^j\frac{4}{\sqrt{\pi}\hat{J}_f}V_C(k)\times\rho_A^{000}(k)\rho_a^{j_p0j_p}(k,\kappa), \tag{21}$$

$$\rho_a^{j_p0j_p}(k,\kappa)=\int_0^\infty drr^2j_0(kr)\rho_a^{j_p0j_p}(r,\kappa),$$

$$\rho_A^{000}(k)=\int_0^\infty drr^2j_0(kr)\rho_A^{000}(r),$$

$$V_C(k)=\int_0^\infty drr^2j_0(kr)4\pi V_C(r).$$

Here $\rho_a^{j_p0j_p}(k,\kappa)$, $\rho_A^{000}(k)$, and $V_C(k)$ are Fourier transforms of the projectile transition density $\rho_a^{j_p0j_p}(r,\kappa)$, the target density $\rho_A^{000}(r)$ and the central part $V_C(r)$ of the *NN* forces between projectile and target nucleons, respectively. A transition density is a reduced matrix element between the initial and final nuclear states and describes the system response to a zero-range perturbation

$$\rho_a^{l_psj_p}(r,\kappa)=\langle\Psi_{\gamma J_f}(\kappa)\|\sum_p\frac{\delta(r-r_p)}{r_p^2}\times[Y_{l_p}(\hat{\boldsymbol{r}}_p)\otimes\sigma_p^s]_{j_p}\|\Psi_{J_i}\rangle, \tag{22}$$

$$\rho_A^{l_tsj_t}(r)=\langle\Phi_{J_A}\|\sum_t\frac{\delta(r-r_t)}{r_t^2}[Y_{l_t}(\hat{\boldsymbol{r}}_t)\otimes\sigma_t^s]_{j_t}\|\Phi_{J_A}\rangle, \tag{23}$$

where summation over $p(t)$ includes all nucleons in the projectile (target). In cluster three-body models the nucleon degrees of freedom are treated unsymmetrically. Only the motion of the two halo nucleons is singled out explicitly in the three-body wave functions while the motion of the core nucleons are combined into the core-center mass and internal motion inside the cluster. The detailed descriptions of the contributions to transition densities from halo nucleons are given in Ref. [15] and the treatment of core nucleon degrees of freedom is presented in Sec. II F. Taking into account these definitions and using the partial wave decomposition of the distorted waves $\chi^{(+)}(\boldsymbol{k}_i,\boldsymbol{R})$

$$\chi^{(+)}(\boldsymbol{k}_i,\boldsymbol{R})=\frac{4\pi}{k_ir}\sum_{l_am_{l_a}}\imath^{l_a}Y^*_{l_am_{l_a}}(\hat{\boldsymbol{k}}_i)Y_{l_am_{l_a}}(\hat{\boldsymbol{R}})\chi_{l_a}(k_i,R), \tag{24}$$

where $\chi_{l_a}(k_i,R)$ is the radial part, the reaction amplitude $T_\delta(\boldsymbol{k}_f,\boldsymbol{k}_i,\kappa)$ can be written as

$$T_\delta(\boldsymbol{k}_f,\boldsymbol{k}_i,\kappa)=\frac{1}{\pi^{3/2}k_ik_f}\sum_{j_pJ_tl_al_b}(J_iM_ij_pm_p|J_fM_f)\times(J_AM_{A'}j_tm_t|J_AM_A)(lm_lj_tm_t|j_pm_p)\times(l_bm_{l_b}lm_l|l_am_{l_a})Y^*_{l_am_{l_a}}(\hat{\boldsymbol{k}}_i)Y_{l_bm_{l_b}}(\hat{\boldsymbol{k}}_f)\times\frac{1}{\hat{j}_p\hat{l}_a^2}T^{lj_tj_p,\delta}_{l_b,l_a}(k_f,k_i,\kappa), \tag{25}$$

$$T^{lj_tj_p,\delta}_{l_b,l_a}(k_f,k_i,\kappa)=\imath^{l_a-l-l_b}\hat{j}_p\hat{l}\hat{l}_a\hat{l}_b(l_b0\,l0|l_a0)\times I^{lj_tj_p,\delta}_{l_b,l_a}(k_f,k_i,\kappa), \tag{26}$$

where the radial integrals $I^{lj_tj_p,\delta}_{l_b,l_a}$ are defined as

$$I^{lj_tj_p,\delta}_{l_b,l_a}(k_f,k_i,\kappa)=(2\pi)^3\int_0^\infty dR\chi_{l_b}(k_f,R)\times F^{\delta}_{lj_tj_p}(R,\kappa)\chi_{l_a}(k_i,R). \tag{27}$$

Using Eqs. (17) and (25) in Eq. (12) and performing summation over spin projections, the expression for the exclusive cross section with the momentum and energy of all particles measured, can be obtained,

$$\frac{d^8\sigma_{el}}{d\hat{\boldsymbol{k}}_f d\hat{\boldsymbol{k}}_x d\hat{\boldsymbol{k}}_y d\varepsilon_y dE_\kappa} = \frac{1}{\varepsilon_i\varepsilon_f}\frac{k_f}{k_i}\left(\frac{\mu_x\mu_y}{\hbar^4}\right)^{3/2} 2\sqrt{\varepsilon_y(E_\kappa-\varepsilon_y)} \sum_{S_f,j_t,L_x,L_y,L_a,L_b,L} \frac{(-1)^{J_i+S_f+j_t}}{4\pi\hat{j}_t^2\hat{J}_i^2}$$

$$\times([Y_{L_x}(\hat{\boldsymbol{k}}_x)\otimes Y_{L_y}(\hat{\boldsymbol{k}}_y)]_L\cdot[Y_{L_a}(\hat{\boldsymbol{k}}_i)\otimes Y_{L_b}(\hat{\boldsymbol{k}}_f)]_L)\sum_{\beta,\beta'}(-1)^{l_x+l_y+L_f+J_f+J_f'+l_a+l_a'}$$

$$\times(\hat{l}_b\hat{l}_x\hat{l}_y\hat{L}_f\hat{J}_f^2)(\hat{l}_b'\hat{l}_x'\hat{l}_y'\hat{L}_f'\hat{J}_f'^2)(l_x0\,l_x'0|L_x0)(l_y0\,l_y'0|L_y0)(l_a0\,l_a'0|L_a0)(l_b0\,l_b'0|L_b0)$$

$$\times\begin{Bmatrix} L_f & L_f' & L \\ J_f' & J_f & S_f \end{Bmatrix}\begin{Bmatrix} J_f & J_f' & L \\ j_p' & j_p & J_i \end{Bmatrix}\begin{Bmatrix} j_p & j_p' & L \\ l' & l & j_t \end{Bmatrix}\begin{Bmatrix} l_y' & l_x' & L_f' \\ l_y & l_x & L_f \\ L_y & L_x & L \end{Bmatrix}\begin{Bmatrix} l_a' & l_b' & l' \\ l_a & l_b & l \\ L_a & L_b & L \end{Bmatrix}$$

$$\times\imath^{-(K_f-K_f')}\psi^{l_xl_y}_{K_f}(\alpha_\kappa)\psi^{l_x'l_y'}_{K_f'}(\alpha_\kappa)T^{lj_tj_p,\delta}_{l_b,l_a}(k_f,k_i,\kappa)T^{l'j_tj_p',\delta'*}_{l_b',l_a'}(k_f,k_i,\kappa). \tag{28}$$

Here $\beta=(l_x,l_y,L_f,J_f,K_f,l_a,l_b,l,j_p)$ is a short notation for a set of the quantum numbers characterizing different motion modes in the system. This cross section contains the most complete information that can be extracted from a reaction with unpolarized nuclei. We can calculate this observable but at present time there is no experimental data to be compared with. Also, Eq. (28) depends on too many variables to offer a meaningful analysis of the important correlations. More instructive is to integrate out most of the independent variables and analyze various inclusive cross sections that can be compared with experiment, and thus clarify the underlying dynamics on which the model is based. At the moment we restrict our analysis to inclusive cross sections that are not more than double folded. Even so, many different energy and angular correlations can be singled out that contain valuable information about the nuclear structure of halo nuclei and the reaction mechanisms.

After fragmentation there are four different, physically meaningful momenta: $\boldsymbol{k}_i$ is the momentum of initial beam, $\boldsymbol{k}_f$ is the momentum of relative motion between c.m. of projectile and target, $\boldsymbol{k}_x$ and $\boldsymbol{k}_y$ are the relative momenta between fragments in the projectile rest frame. The beam momentum $\boldsymbol{k}_i$ is fixed by initial conditions and memory about its value and direction is kept in the system through conservation laws, but the other momenta can be independent variables in terms of which dynamical correlations might be expressed. Keeping absolute values of the single momenta k_f, k_x, or k_y and integrating out other degrees of freedom, the energy distributions $d\sigma/dE_\kappa$, $d\sigma/d\varepsilon_x$, or $d\sigma/d\varepsilon_y$ can be obtained. These describe the total projectile excitation spectrum, the energy distribution of relative motion between two fragments or the energy distribution of one fragment, respectively. Integrating out any two of the three independent momenta $\boldsymbol{k}_f$, $\boldsymbol{k}_y$, or $\boldsymbol{k}_x$, the cross sections become dependent on the angle between the beam direction $\boldsymbol{k}_i$ and the direction of the remaining momentum. Thus, the differential cross section $d^2\sigma/d\Omega_f$, the fragment relative $d^3\sigma/d\boldsymbol{k}_x$, and the fragment momentum distributions $d^3\sigma/d\boldsymbol{k}_y$ can be obtained. An additional integration over two of the three momentum projections gives the usual longitudinal and transverse distributions.

A next class of cross sections can be calculated if only one of the three independent momenta is integrated out. From the possible variants only one, that where an integration over $\boldsymbol{k}_f$ is performed, will be considered below. The vectors $\boldsymbol{k}_x$ and $\boldsymbol{k}_y$, describing the motion of projectile fragments, lie in a plane. After averaging over $\boldsymbol{k}_f$ only the angle between $\boldsymbol{k}_x$ and $\boldsymbol{k}_y$ has a physical meaning, the orientation of the plane they define does not play any role and can be integrated out. The resulting angular correlations $d\sigma/d(\hat{\boldsymbol{k}}_x\cdot\hat{\boldsymbol{k}}_y)$ might be of interest.

A variety of the different motion modes connected with any momentum $\boldsymbol{k}$, are characterized by some subset of quantum numbers and coexist in the final system. All of them interfere with each other and give a coherent contribution to the exclusive cross sections (28). Integration over the momentum destroys the interference and the corresponding motion modes add independent contributions to the cross sections. Therefore, different cross sections are sensitive to different correlations, and simultaneous descriptions of all of them within the framework of one model gives a thorough test of the underlying dynamics and model assumptions on nuclear structure and reaction mechanisms.

Integrating over all independent variables except for the projectile excitation energy E_κ and taking into account the orthogonality properties of hyperharmonics

$$\int_0^{E_\kappa} d\varepsilon_y\sqrt{\varepsilon_y(E_\kappa-\varepsilon_y)}\,\psi^{l_xl_y}_K(\alpha_\kappa)\psi^{l_xl_y}_{K'}(\alpha_\kappa)=2E_\kappa^2\delta_{KK'}, \tag{29}$$

the spectrum of inelastic excitations in the halo nucleus can be written as

$$\frac{d\sigma_{el}}{dE_\kappa}=\frac{1}{\varepsilon_i\varepsilon_f}\frac{k_f}{k_i}\left(\frac{\mu_x\mu_y}{\hbar^4}\right)^{3/2}4E_\kappa^2 \times\sum_{S_f,j_t,\beta}\frac{\hat{J}_f^2}{\hat{l}^2\hat{j}_t^2\hat{j}_p^2\hat{l}_a^2\hat{J}_i^2}|T^{lj_tj_p,\delta}_{l_b,l_a}(k_f,k_i,\kappa)|^2, \tag{30}$$

which describes the strength distribution of the different motion modes over total projectile excitation energy E_κ. The factor E_κ^2, which originates from the three-body phase volume, guarantees the correct cross-section behavior at the breakup threshold. All correlations between modes are lost and they give independent contributions to the cross section. The fragment energy distributions $[\beta=(\eta,K_f)]$

$$\frac{d^2\sigma_{el}}{d\varepsilon_y dE_\kappa}=\frac{d^2\sigma_{el}}{d\varepsilon_x dE_\kappa}$$
$$=\frac{1}{\varepsilon_i\varepsilon_f}\frac{k_f}{k_i}\left(\frac{\mu_x\mu_y}{\hbar^4}\right)^{3/2}2\sqrt{\varepsilon_y(E_\kappa-\varepsilon_y)}$$
$$\times\sum_{S_f,j_t,\eta,K_f,K_f'}\frac{\hat J_f^2}{\hat l^2\hat j_t^2\hat j_p^2\hat l_a^2\hat j_i^2}\imath^{-(K_f-K_f')}\psi_{K_f}^{l_xl_y}(\alpha_\kappa)$$
$$\times\psi_{K_f'}^{l_xl_y}(\alpha_\kappa)T_{l_b,l_a}^{lj_tj_p,\delta}(k_f,k_i,\kappa)T_{l_b,l_a}^{lj_tj_p,\delta'*}(k_f,k_i,\kappa) \tag{31}$$

carry the energy correlations in the fragment motion that is contained in interference between modes with different values of the hypermoment K_f. For a single-fragment energy distribution we have to integrate over the total excitation energy E_κ. In spite of the equality of the double-folded cross sections, the single distributions $d\sigma_{el}/d\varepsilon_y$ and $d\sigma_{el}/d\varepsilon_x$ will be different, since the integration over E_κ is equivalent to the different projections from the two-dimensional distribution over ε_y and ε_x.

The differential cross section for the projectile c.m. scattering with fixed inelastic excitation energy E_κ can be written as

$$\frac{d^3\sigma_{el}}{d\hat{\boldsymbol{k}}_f dE_\kappa}=\frac{1}{\varepsilon_i\varepsilon_f}\frac{k_f}{k_i}\left(\frac{\mu_x\mu_y}{\hbar^4}\right)^{3/2}4E_\kappa^2$$
$$\times\sum_{L,l,j_t,j_p,\delta}\frac{\hat J_f^2}{4\pi\hat l^2\hat j_t^2\hat j_p^2\hat j_i^2}P_L(\hat{\boldsymbol{k}}_i\cdot\hat{\boldsymbol{k}}_f)(-1)^l\hat l_b\hat l_b'$$
$$\times(l_a0\,l_a'0|L0)(l_b0\,l_b'0|L0)$$
$$\times\begin{Bmatrix}l_a & l_a' & L\\ l_b' & l_b & l\end{Bmatrix}T_{l_b,l_a}^{lj_tj_p,\delta}(k_f,k_i,\kappa)$$
$$\times T_{l_b',l_a'}^{lj_tj_p,\delta*}(k_f,k_i,\kappa). \tag{32}$$

Here, any mode of internal excitation, characterized by the quantum numbers δ, gives an independent contribution to the differential distribution.

In the projectile rest frame $\boldsymbol{k}_1+\boldsymbol{k}_2+\boldsymbol{k}_3=0$, used for the representation of fragment momentum distributions, the momentum $\boldsymbol{k}_3$ of the projectile constituent 3 is equal to the Jacobi momentum $\boldsymbol{k}_y$. Hence, integration of the exclusive cross section over variables $\hat{\boldsymbol{k}}_x$ and $\hat{\boldsymbol{k}}_f$ of the unobserved particles and summation over all spin and angular momentum projections, gives the elastic fragmentation cross section for momentum distribution of the projectile particle 3, which can be written as follows:

$$\frac{d^4\sigma_{el}}{d\boldsymbol{k}_y dE_\kappa}=\frac{1}{\varepsilon_i\varepsilon_f}\frac{k_f}{k_i}\left(\frac{\mu_x}{\hbar^2}\right)^{3/2}\sqrt{2(E_\kappa-\varepsilon_y)}\sum_{S_f,j_t,l_x,l_b,L}\frac{(-1)^{J_i+S_f+j_t+l_x+l_b}}{4\pi\hat J_i^2\hat j_t^2}P_L(\hat{\boldsymbol{k}}_i\cdot\hat{\boldsymbol{k}}_y)\sum_{l_y,\lambda,l_y',\lambda'}(-1)^{J_f+J_f'+l+l'}(\hat l_y\hat L_f\hat J_f^2)$$
$$\times(\hat l_y'\hat L_f'\hat J_f'^2)(l_y0\,l_y'0|L0)(l_a0\,l_a'0|L0)\begin{Bmatrix}l_y & l_y' & L\\ L_f' & L_f & l_x\end{Bmatrix}\begin{Bmatrix}L_f & L_f' & L\\ J_f' & J_f & S_f\end{Bmatrix}\begin{Bmatrix}J_f & J_f' & L\\ j_p' & j_p & J_i\end{Bmatrix}\begin{Bmatrix}j_p & j_p' & L\\ l' & l & j_t\end{Bmatrix}\begin{Bmatrix}l & l' & L\\ l_a' & l_a & l_b\end{Bmatrix}$$
$$\times\imath^{-(K_f-K_f')}\psi_{K_f}^{l_xl_y}(\alpha_\kappa)\psi_{K_f'}^{l_xl_y'}(\alpha_\kappa)T_{l_b,l_a}^{lj_tj_p,\delta}(k_f,k_i,\kappa)T_{l_b,l_a'}^{l'j_tj_p',\delta'*}(k_f,k_i,\kappa). \tag{33}$$

Here $\lambda=\{J_f,L_f,K_f,j_p,l,l_a\}$, and the motion modes characterized by (l_y,λ) quantum numbers give a coherent contribution to the cross section. For momentum distribution of relative motion between two fragments, we have to study distribution over $\hat{\boldsymbol{k}}_x$ momentum,

$$\frac{d^4\sigma_{el}}{d\boldsymbol{k}_x dE_\kappa}=\frac{1}{\varepsilon_i\varepsilon_f}\frac{k_f}{k_i}\left(\frac{\mu_y}{\hbar^2}\right)^{3/2}\sqrt{2(E_\kappa-\varepsilon_x)}\sum_{S_f,j_t,l_y,l_b,L}\frac{(-1)^{J_i+S_f+j_t+l_y+l_b}}{4\pi\hat J_i^2\hat j_t^2}P_L(\hat{\boldsymbol{k}}_i\cdot\hat{\boldsymbol{k}}_x)\sum_{l_x,\beta,l_x',\beta'}(-1)^{J_f+J_f'+l+l'}(\hat l_x\hat L_f\hat J_f^2)(\hat l_x'\hat L_f'\hat J_f'^2)$$
$$\times(l_x0\,l_x'0|L0)(l_a0\,l_a'0|L0)\begin{Bmatrix}l_x & l_x' & L\\ L_f' & L_f & l_y\end{Bmatrix}\begin{Bmatrix}L_f & L_f' & L\\ J_f' & J_f & S_f\end{Bmatrix}\begin{Bmatrix}J_f & J_f' & L\\ j_p' & j_p & J_i\end{Bmatrix}\begin{Bmatrix}j_p & j_p' & L\\ l' & l & j_t\end{Bmatrix}\begin{Bmatrix}l & l' & L\\ l_a' & l_a & l_b\end{Bmatrix}$$
$$\times\imath^{-(K_f-K_f')}\psi_{K_f}^{l_xl_y}(\alpha_\kappa)\psi_{K_f'}^{l_x'l_y}(\alpha_\kappa)T_{l_b,l_a}^{lj_tj_p,\delta}(k_f,k_i,\kappa)T_{l_b,l_a'}^{l'j_tj_p',\delta'*}(k_f,k_i,\kappa). \tag{34}$$

The expressions (33) and (34) are starting points for calculations of the transverse and longitudinal fragment-momentum distributions. The way to do this will be discussed below. Performing integrations of these expressions over energies for fixed values of $((\hat{\boldsymbol{k}}_i\cdot\hat{\boldsymbol{k}}_y)(\hat{\boldsymbol{k}}_i\cdot\hat{\boldsymbol{k}}_x))$, the fragment (momentum of relative motion between fragments) angular distributions relative beam direction, in the projectile rest frame, can be obtained.

Finally, the triple cross section for angular correlations can be written

$$\frac{d^3\sigma_{el}}{d(\hat{\boldsymbol{k}}_x\cdot\hat{\boldsymbol{k}}_y)d\varepsilon_y dE_\kappa}=\frac{1}{\varepsilon_i\varepsilon_f}\frac{k_f}{k_i}\left(\frac{\mu_x\mu_y}{\hbar^2}\right)^{3/2}2\sqrt{\varepsilon_y(E_\kappa-\varepsilon_y)}\sum_{\epsilon,L}\frac{\hat{J}_f^2}{\hat{l}^2\hat{j}_t^2\hat{j}_p^2\hat{l}_a^2\hat{j}_i^2}\frac{(-1)^{L_f+L}}{2}P_L(\hat{\boldsymbol{k}}_x\cdot\hat{\boldsymbol{k}}_y)$$
$$\times\sum_{l_x,l_y,K_f,l_x',l_y',K_f'}\hat{l}_x\hat{l}_y\hat{l}_x'\hat{l}_y'(l_x0\,l_x'0|L0)(l_y0\,l_y'0|L0)\begin{Bmatrix}l_x & l_x' & L\\ l_y' & l_y & L_f\end{Bmatrix}$$
$$\times\imath^{-(K_f-K_f')}\psi_{K_f}^{l_xl_y}(\alpha_\kappa)\psi_{K_f'}^{l_x'l_y'}(\alpha_\kappa)T_{l_b,l_a}^{l_jt_jp,\delta}(k_f,k_i,\kappa)T_{l_b,l_a}^{l_jt_jp,\delta'}{}^*(k_f,k_i,\kappa),\tag{35}$$

where $\epsilon=(l,j_t,j_p,l_a,l_b,L_f,S_f,J_f)$. All projectile excitations with the different orbital L_f, spin S_f, and total angular momentum J_f are summed independently here, while keeping the correlations in the relative fragment motion. Integrating additionally over the energies ε_y and E_κ, the angular correlations $d\sigma_{el}/d(\hat{\boldsymbol{k}}_x\cdot\hat{\boldsymbol{k}}_y)$ can be calculated.

C. Inelastic breakup

The exclusive inelastic breakup cross section (11) (when energies and momenta of all particles are observed), averaged over initial and summed over final spin projections, can be written as

$$\frac{d^6\sigma_{in}}{d\hat{\boldsymbol{k}}_x d\boldsymbol{k}_y dE_\kappa}=(2\pi)^4\frac{\mu_i}{k_i\hbar^2}\sqrt{2}\left(\frac{\mu_x}{\hbar^2}\right)^{3/2}\sqrt{E_\kappa-\varepsilon_y}$$
$$\times\int d\boldsymbol{R}\frac{1}{\pi}[-\mathrm{Im}\tilde{U}_{aA}(\boldsymbol{R})]\frac{1}{\hat{J}_i^2\hat{J}_A^2}$$
$$\times\sum_{m_1,m_2,M_{A'},M_i,M_A}|T_{in}(\boldsymbol{R})|^2.\tag{36}$$

The matrix element T_{in} for inelastic fragmentation has a form similar to Eq. (13) for the elastic breakup, and is given by

$$T_{in}(\boldsymbol{R})=\langle G(\boldsymbol{R},\varepsilon_f),\Phi_{J_AM_{A'}},\Psi_{m_1,m_2}^{(-)}(\boldsymbol{k}_x,\boldsymbol{k}_y)|$$
$$\times\sum_{p,t}V_{pt}|\Psi_{J_iM_i},\Phi_{J_AM_A},\chi^{(+)}(\boldsymbol{k}_i)\rangle,\tag{37}$$

where the optical-model Green's function $G(\boldsymbol{R},\boldsymbol{R}',\varepsilon_f)$ replaces the distorted wave $\chi(\boldsymbol{k}_f,\boldsymbol{R}')$ for an exit channel. The Green's function $G(\boldsymbol{R},\boldsymbol{R}',\varepsilon_f)$ is the solution of the equation

$$\left(\varepsilon_f+\frac{\hbar^2}{2\mu_f}\nabla^2-\tilde{U}_{aA}\right)G(\boldsymbol{R},\boldsymbol{R}',\varepsilon_f)=\delta(\boldsymbol{R}-\boldsymbol{R}')\tag{38}$$

with the same energy $\varepsilon_f=\varepsilon_i-E_\kappa-Q$ as for the relative motion in the exit channel in elastic fragmentation. For a central optical potential $\tilde{U}_{aA}(R)$, the Green's function G has the following partial-wave decomposition:

$$G(\boldsymbol{R},\boldsymbol{R}',\varepsilon_f)=\frac{2\mu_f}{\hbar^2}\sum_l\frac{1}{rr'}G_l(R,R',k_f)Y_{lm}(\hat{\boldsymbol{R}})Y_{lm}(\hat{\boldsymbol{R}}')^*,\tag{39}$$

where the radial part $G_l(R,R',k_f)$ can be represented as a product of the regular $\chi_l(k_f,R)$ and outgoing $h_l(k_f,R)$ radial solutions in the optical potential $\tilde{U}_{aA}(R)$,

$$G_l(R,R',k_f)=\frac{\chi_l(k_f,R_<)h_l(k_f,R_>)}{W(\chi_l,h_l)}.\tag{40}$$

Here $R_<$ and $R_>$ mean the smallest and largest of the coordinates R and R', respectively. The

$$W(\chi_l,h_l)=\chi_l\frac{dh_l}{dR}-\frac{d\chi_l}{dR}h_l$$

is the Wronskian of the independent solutions χ_l and h_l.

Inserting the decompositions (14), (24), (19), and (39) into Eq. (36) and doing all calculations in a way analogous to that for elastic breakup, the cross sections for different energy and angular correlations except for Eq. (32), can be obtained. As an example, the expression for a particle momentum distribution becomes

$$\frac{d^4\sigma_{in}}{d\boldsymbol{k}_y dE_\kappa}=\frac{1}{\varepsilon_i\varepsilon_f}\frac{k_f}{k_i}\left(\frac{\mu_x}{\hbar^2}\right)^{3/2}\sqrt{2(E_\kappa-\varepsilon_y)}\int_0^\infty dR\,\mathrm{Im}\left(-\frac{2\mu_f}{\hbar^2}\tilde{U}_{aA}(R)\right)\sum_{S_f,j_t,l_x,l_b,L}P_L(\hat{\boldsymbol{k}}_i\cdot\hat{\boldsymbol{k}}_y)\frac{(-1)^{J_i+S_f+j_t+l_x+l_b}}{4\pi\hat{J}_i^2\hat{j}_t^2}$$

$$\times\sum_{l_y,\lambda,l_y',\lambda'}(-1)^{J_f+J_f'+l+l'}(\hat{l}_y\hat{L}_f\hat{J}_f^2)(\hat{l}_y'\hat{L}_f'\hat{J}_f'^2)(l_y0\,l_y'0|L0)(l_a0\,l_a'0|L0)$$

$$\times\begin{Bmatrix} l_y & l_y' & L\\ L_f' & L_f & l_x\end{Bmatrix}\begin{Bmatrix} L_f & L_f' & L\\ J_f' & J_f & S_f\end{Bmatrix}\begin{Bmatrix} J_f & J_f' & L\\ j_p' & j_p & J_i\end{Bmatrix}\begin{Bmatrix} j_p & j_p' & L\\ l' & l & j_t\end{Bmatrix}\begin{Bmatrix} l & l' & L\\ l_a' & l_a & l_b\end{Bmatrix}$$

$$\times\imath^{-(K_f-K_f')}\psi_{K_f}^{l_xl_y}(\alpha_\kappa)\psi_{K_f'}^{l_xl_y'}(\alpha_\kappa)\tilde{T}_{l_b,l_a}^{lj_tj_p,\delta}(R,k_f,k_i,\kappa)\tilde{T}_{l_b,l_a'}^{l'j_tj_p',\delta^*}(R,k_f,k_i,\kappa), \tag{41}$$

where the amplitude $\tilde{T}_{l_b,l_a}^{lj_tj_p,\delta}(R,k_f,k_i,\kappa)$ has the same expression as $T_{l_b,l_a}^{lj_tj_p,\delta}(k_f,k_i,\kappa)$ in Eq. (26), but with $I_{l_b,l_a}^{lj_tj_p,\delta}(k_f,k_i,\kappa)$ replaced by a new radial integral

$$\tilde{T}_{l_b,l_a}^{lj_tj_p,\delta}(R,k_f,k_i,\kappa)=(2\pi)^{3/2}\int_0^\infty dR'\,G_{l_b}(R,R',k_f)F_{lj_tj_p}^{\delta}\times(R',\kappa)\chi_{l_a}(k_i,R'). \tag{42}$$

The expressions (33) and (41) for particle momentum distribution in elastic and inelastic breakup have the same dependence on different quantum numbers describing the relative motion of decaying fragments. In addition, the integrand expression in Eq. (41) gives the cross-section distribution of inelastic fragmentation as a function of the radial coordinate R.

D. Longitudinal and transverse momentum distributions

We now use a Jacobi coordinate system where the momentum direction $\hat{\boldsymbol{k}}_y$ in the projectile rest frame is equal to that of the momentum of the observed fragment $\hat{\boldsymbol{k}}_3$.

To calculate the *longitudinal momentum distribution*, we have to fix the projection k_z of the momentum $\boldsymbol{k}_y=\boldsymbol{k}_3$ onto the beam direction $\hat{\boldsymbol{k}}_i$ in Eqs. (33) and (41) and integrate over the other momentum components. Due to azimuthal symmetry, the integration is reduced to one dimension, over the orthogonal $k_\perp$ component of the total momentum $|\boldsymbol{k}_y|=\sqrt{k_z^2+k_\perp^2}$,

$$\frac{d^2\sigma}{dk_z dE_\kappa}=\int_0^{[(2\mu_y/\hbar^2)E_\kappa-k_z^2]^{1/2}}dk_\perp k_\perp\sqrt{\frac{2\mu_y}{\hbar^2}E_\kappa-k_z^2-k_\perp^2}\times\sum_{\substack{L,l_x,l_y\\K_f,l_y',K_f'}}\mathcal{F}\times\psi_{K_f}^{l_xl_y}(\alpha_\kappa)\psi_{K_f'}^{l_xl_y'}(\alpha_\kappa)P_L\left(\frac{k_z}{\sqrt{k_z^2+k_\perp^2}}\right). \tag{43}$$

Here $\mathcal{F}$ includes the transition form factors and does not depend on $k_\perp$.

For the *transverse momentum distribution*, we have to fix the momentum projection k_x perpendicular to the beam direction $\hat{\boldsymbol{k}}_i$ and integrate over other momentum components. To this end, it is convenient to combine the k_y and k_z components of the vector $\boldsymbol{k}_y$ to a $k_\perp=\sqrt{k_y^2+k_z^2}$, which is lying in the (y,z) plane and has an angle ϕ relative to the axis $\hat{\boldsymbol{z}}\|\hat{\boldsymbol{k}}_i$. Then the transverse momentum distribution is

$$\frac{d^2\sigma}{dk_x dE_\kappa}=\int_0^{[(2\mu_y/\hbar^2)E_\kappa-k_x^2]^{1/2}}dk_\perp k_\perp\sqrt{\frac{2\mu_y}{\hbar^2}E_\kappa-k_x^2-k_\perp^2}\times\sum_{\substack{L,l_x,l_y\\K_f,l_y',K_f'}}\mathcal{F}\psi_{K_f}^{l_xl_y}(\alpha_\kappa)\psi_{K_f'}^{l_xl_y'}(\alpha_\kappa)\times\int_0^{2\pi}d\phi P_L\left(\frac{k_\perp\cos\phi}{\sqrt{k_x^2+k_\perp^2}}\right). \tag{44}$$

For odd L the integral over ϕ gives zero and has a simple polynomial form for even values. The expressions (43) and (44) define longitudinal and transverse momentum distributions for fixed projectile excitation energy E_κ. The integration of a product of hyperharmonics and Legendre polynomial over $k_\perp$ can be done analytically and can be reduced to the sums of incomplete beta functions. Usually the experimental data include contributions for all excitation energies E_κ allowed by the experimental setup. Hence, we need additionally to integrate the momentum distributions over excitation energy from the breakup threshold up to some maximal energy defined by experimental conditions.

Formulas (43) and (44) give the distributions for particle 3 in the projectile rest frame. In order to get the distributions of particles 1 and 2 we have to rotate to the other sets of Jacobi coordinates where $\boldsymbol{k}_y=\boldsymbol{k}_{1,2}$; a change that is easily done since the amplitudes transform through Raynal-Revai coefficients in the hyperspherical method [31]. Hence the momentum distributions have the same structure for core and halo neutrons.

Before discussing the numerical results it is useful to make a few remarks concerning the basic structure of formulas (33) and (41). The expressions describe the momentum distribution of the constituents of the projectile relative to the

only direction (beam) of which memory still exists in the reaction after integration over unobserved particle coordinates. As a result, the cross sections (33) and (41) depend only on the angle between the beam and the detected particle. This dependence is described by the Legendre polynomial $P_L(\hat{\boldsymbol{k}}_y \cdot \hat{\boldsymbol{k}}_i)$ and the cross sections are incoherent sums over quantum numbers (S_f, j_t, l_x, l_b) that characterize unobserved fragments. The nuclear states have many other quantum numbers and due to the lack of symmetry the corresponding components are connected and give coherent contributions to the cross sections. For nonzero values of L, there are interference terms between excitations with the different total momenta J_f reached by the different transferred momenta j_p. The interference is expressed in different ways for the longitudinal [Eq. (43)] and transverse [Eq. (44)] distributions. For the longitudinal distributions all orders L of the Legendre polynomial $P_L(\hat{\boldsymbol{k}}_i \cdot \hat{\boldsymbol{k}}_y)$, allowed by the angular momentum addition rules, give contributions. For the transverse, only even values of L are present. For even L, the interference terms are the same for the positive and negative values of $k_{x,z}$ and have the opposite signs for odd. *As a result, the transverse distributions always have symmetrical shape relative the origin of the k_x axis, while the longitudinal one may be asymmetric relative to $k_z=0$.* All interference terms should belong to the same values of the orbital angular momentum l_x and odd L may appear only for l_y with different parity. Hence, the interference between nuclear states with different parity excited at the same energy with comparable intensity may cause deviations from the symmetrical shape in the longitudinal distributions. Studying such distortions may give valuable information on the structure of halo nuclei. Recently, in the longitudinal momentum distributions of ^{7}Be produced in Coulomb breakup of the ^{8}B (a candidate for one-proton halo nucleus), large asymmetry arising from interference of $E1$ and $E2$ excitations was measured [32] and discussed, for example, in Ref. [33].

E. Treatment of Coulomb interaction

For a consistent treatment of electromagnetic dissociation, Coulomb and nuclear interactions have to be treated on equal footing. The interaction V_{pt} between projectile and target nucleons has a short-range part due to strong forces but the central part also includes Coulomb repulsion when both nucleons are protons. In calculations of the radial form factor (21) performed in momentum space, the central part $V_C(k)$ of the nucleon-nucleon forces acting between protons has a nuclear part together with a Coulomb part $V_{Coul}(k) = 4\pi e^2/k^2$, which causes destructive interference with nuclear attraction. The long-range nature of Coulomb forces is a main feature and involves additional effects in comparison with heavy-ion reaction calculations that only include nuclear interaction. For short-range nuclear forces it is sufficient to calculate the nuclear form factor (21) within a finite region $0 \leqslant R \leqslant R_{max}$ of coordinate space outside of which the form factor becomes negligible. Accordingly, only a restricted number $l < L_N$ of distorted partial waves have to be taken into account in reaction calculations. In the presence of long-range Coulomb interaction, the form factor has a slowly decreasing tail that reaches out to a much larger radii. For a target with high charge, the tail has sufficient amplitude to cause a strong Coulomb dissociation. As a result, there is a slow convergence of the partial-wave decomposition and it is necessary to extend the radial integration in Eqs. (27) and (42) to large distances. A simplification is that at $R \geqslant R_{max}$ the Coulomb form factor is known analytically and has a simple form

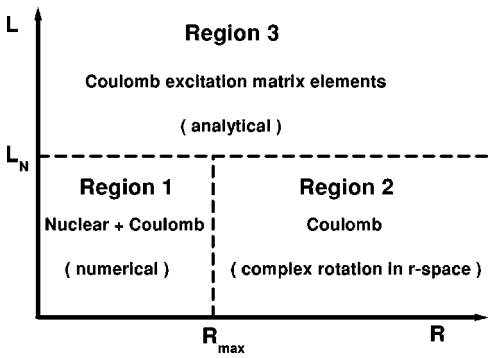

FIG. 2. Separation of the coordinate and distorted-wave spaces into regions where different methods are used for the calculations of radial integrals.

$$F^{\delta}_{j_p 0 j_p}(R,\kappa)\big|_{r>R_{max}} = i^{j_p} \frac{4\pi e^2 Z_A}{(2j_p+1)\hat{J}_f} \langle \Psi_{\gamma J_f}(\kappa) \| \sum_{p=1}^{Z_p} r_p^{j_p} Y_{j_p}(\hat{r}_p) \| \Psi_{J_i} \rangle \times \frac{1}{R^{j_p+1}}. \tag{45}$$

Hence, we calculate Eq. (21) only for $R \leqslant R_{max}$ and use the analytic form factor (45) for larger radii. The coordinate and partial-wave spaces can be separated (as shown in Fig. 2) into three regions [34] where different methods of the radial integration are used. The first region ($R \leqslant R_{max}$ and $l \leqslant L_N$) is for calculations where a short-range nuclear and a long-range Coulomb interactions are present. In this region the distorted waves and form factors are known numerically and numerical integration of the radial integrals has a sufficient accuracy. The second region corresponds to the low partial waves $l \leqslant L_N$ and radial integrations from $R_{max} < R < \infty$. The form factor is known analytically [Eq. (45)], the distorted waves are given by their asymptotic representations and their overlaps are non-negligible, if Coulomb excitation is significant. The poor convergence of numerical integrations can be handled by the method of contour integration in the complex radial plane [35] since all functions are known analytically. The third region embraces the high partial waves $l > L_N$. The partial waves do not penetrate the large centrifugal barrier, therefore these waves do not feel the nuclear potential and experience only Rutherford scattering and are the regular Coulomb wave functions. Since these partial waves are negligible at small R, the analytical form-factor expression (45) can be used also at $R \leqslant R_{max}$. Then the radial integrals are reduced to the well-known integrals of Coulomb excitation

theory [36] with explicit analytical expressions in terms of the hypergeometric functions. With increasing partial wave orbital angular momentum, the Coulomb matrix elements decrease exponentially [36], but the rate of convergence depends strongly on the excitation energy and is rather slow near the breakup threshold. For example, in the case of the low-energy dipole excitations for ^{6}He fragmentation on ^{208}Pb at 240 MeV/nucleon, we have taken into account up to 20 000 partial waves while only about 400 were sufficient for the short-ranged nuclear interaction. This allows us to perform quantum-mechanical calculations of nuclear and Coulomb excitations, including their interference, without artificial separation of different mechanisms. Note that a Coulomb-nuclear interference only appears in region 1 (see Fig. 2), where both nuclear and Coulomb form factors are present. The contributions to the amplitude from region 2 and 3 are purely Coulombic. The degree of interference in cross sections is governed by the magnitude of the contributions from these regions to a total amplitude.

F. Inclusion of nucleon degrees of freedom of the core

In the description of the light systems such as ^{6}He, recoil effects, i.e., translational symmetry play an important role. Thus, from the beginning we have based the formulation of the reaction dynamics on relative, translationally invariant Jacobi coordinates. Within the three-body cluster model only the halo valence neutrons and core c.m. are directly expressed in the relative motion function $\Psi_{\gamma,J_f,M_f}(\boldsymbol{x},\boldsymbol{y},\boldsymbol{\kappa})$ while the coordinates of the core constituents are referred to in a more complex way. The treatment of the degrees of freedom of the core nucleons merits in this context a special attention. Figure 2 shows the coordinate system, relevant to our case. The vectors $\boldsymbol{r}_{1,2}$ and $\boldsymbol{r}_i$ show the positions of the halo and α-core nucleons with respect to the ^{6}He center-of-mass O, while $\boldsymbol{\xi}_i$ is the coordinate of ith core nucleon relative to the core c.m. (point 3). The $\boldsymbol{y}$ and $\boldsymbol{x}$ are Jacobi vectors between c.m. of the neutron pair and the α core and between the halo neutrons. Recall that $\boldsymbol{R}$ is the distance between the collision partners and the variable on which the distorted waves $\chi^{(\pm)}_{i,f}$ depend. The nuclear structure enters in the reaction dynamics as a transition density that describes the response of the system to a zero-range perturbation, and can be expressed as a reduced matrix element between the initial bound $\Psi_{J_iM_i}$ and final continuum $\Psi_{\gamma J_fM_f}$ nuclear states

$$\rho^{lsj}(r)=\langle\Psi_{\gamma J_f}\|\sum_{i=1}^{6}\frac{\delta(r-r_i)}{r_i^2}[Y_l(\hat{\boldsymbol{r}}_i)\otimes\sigma_i^s]_j\|\Psi_{J_i}\rangle$$
$$=\rho_n^{lsj}(r)+\rho_\alpha^{lsj}(r). \tag{46}$$

Here the summation i is over nucleons in the halo nucleus and integration over all coordinates $\boldsymbol{r}_i$ is to be understood. The quantum numbers l, s, and j are relative orbital, spin, and total angular momenta, respectively, transferred to the nucleus in the excitation process. In the second line of Eq. (46), the two parts of the transition density connected to contributions of halo neutrons $\rho_n^{lsj}(r)$ and α-core nucleons $\rho_\alpha^{lsj}(r)$ are shown separately. In the cluster three-body model the nuclear wave functions have the product forms $\Psi_{\gamma JM}=\Phi(\boldsymbol{\xi}_i)\psi_{\gamma JM}(\boldsymbol{x},\boldsymbol{y})$, where $\Phi(\boldsymbol{\xi}_i)$ is an intrinsic core wave function (with zero spin for ^{6}He), while $\psi_{\gamma JM}(\boldsymbol{x},\boldsymbol{y})$ describes relative motion of the cluster constituents (carrying the total angular momentum J). In this model the calculation of halo neutron transition density $\rho_n^{lsj}(r)$ involves the three-body wave function $\psi_{\gamma JM}(\boldsymbol{x},\boldsymbol{y})$, since the halo neutron coordinates $\boldsymbol{r}_{1,2}$ depend only on the Jacobi vectors $\boldsymbol{x}$ and $\boldsymbol{y}$. A detailed scheme for the $\rho_n^{lsj}(r)$ calculation is given in [15,14] (the contributions from the halo neutrons 1 and 2 are equal due to particle identity).

The calculation of the halo neutron transition density $\rho_\alpha^{lsj}(r)$ for the α-core nucleons is more complex. This transition density is defined by the vectors $\boldsymbol{r}_i=\beta\boldsymbol{y}+\boldsymbol{\xi}_i$, shown on Fig. 1, where $\beta=(m_1+m_2)/(m_1+m_2+m_3)$, with $m_1=m_2$ and m_3 being halo neutron and core masses, respectively. The transition density operator in Eq. (46) has to be decomposed into multipoles depending on the coordinates $\beta\boldsymbol{y}$ and $\boldsymbol{\xi}_i$. It is convenient to do the multipole decomposition in momentum space [30,15] where

$$\rho^{lsj}(k)=\int_0^\infty dr\, r^2 j_l(kr)\rho^{lsj}(r)$$
$$=\langle\Psi_{\gamma J_f}\|\sum_i\tau_{lsj}(i)\|\Psi_{J_i}\rangle,$$
$$\tau_{lsj,m}(i)=j_l(kr_i)[Y_l(\hat{\boldsymbol{r}}_i)\otimes\sigma_i^s]_{j,m}. \tag{47}$$

The multipole operator $\tau_{lsj,m}(i)$ for the ith core nucleon can be decomposed in a general way in a product of multipole operators depending separately on $\beta\boldsymbol{y}$ and $\boldsymbol{\xi}_i$,

$$\tau_{lsj,m}(i)=\sqrt{4\pi}\sum_{Ll_yl_\xi}\imath^{l_y+l_\xi-l}\hat{L}\hat{l}_y\hat{l}_\xi(l_y0\,l_\xi0|l0)$$
$$\times(-1)^{l+s-j}\begin{Bmatrix}l & s & j\\ L & l_y & l_\xi\end{Bmatrix}[\tau_{l_y0l_y}(\beta y)$$
$$\otimes\tau_{l_\xi sL}(\xi_i)]_{j,m}. \tag{48}$$

Here a spin transfer s is connected only to operator $\tau_{l_\xi sL}(\xi_i)$ depending on internal cluster coordinates, while operator $\tau_{l_y0l_y}(\beta y)$ acts on the cluster c.m. After taking the matrix element between initial and final nuclear wave functions $\Phi(\boldsymbol{\xi}_i)\psi_{J_i,J_f}(\boldsymbol{x},\boldsymbol{y})$ the nucleon transition density that takes into account an internal structure of the core with any spin can be obtained within the cluster model. For an α-particle core with zero spin and isospin, the result is very simple,

$$\rho_\alpha^{l0l}(k)=\langle\psi_{\gamma J_f}\|j_l(k\beta y)Y_l(\hat{\boldsymbol{y}})\|\psi_{J_i}\rangle\langle\Phi\|\sum_{i=1}^{4}j_0(k\xi_i)\|\Phi\rangle$$
$$=\rho_{\alpha_{cm}}^{l0l}(k)\rho_{mat}(k), \tag{49}$$

where $\rho_{\alpha_{cm}}^{l0l}(k)=\langle\psi_{J_f}\|j_l(k\beta y)Y_l(\hat{\boldsymbol{y}})\|\psi_{J_i}\rangle$ is the transition density for the α-core c.m., while $\rho_{mat}(k)$

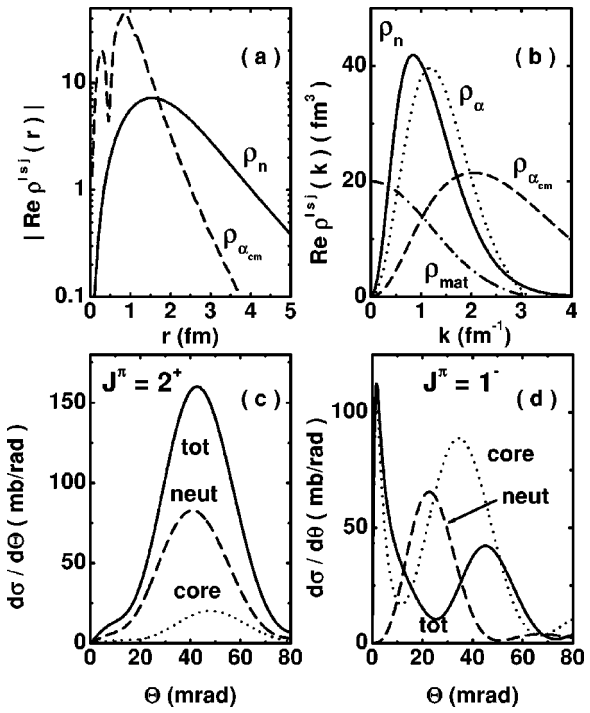

FIG. 3. The real part of the ^{6}He transition density ρ^{lsj} $(l=j=2,s=0)$ for the excitation of the $(KLSl_xl_y)=(22002)$ component of a continuum wave function at 2^+ resonance peak energy $(E^*=1.8$ MeV). (a) Coordinate space. Solid and dashed lines show the modulus of the halo-neutron and α-core c.m. transition densities, respectively. (b) Momentum space. Solid, dashed, and dotted lines show transition densities of the halo neutrons, α-core c.m. motion, and core nucleons transition densities, respectively. The dashed-dotted line shows the α-particle matter density in arbitrary units. Theoretical angular distributions are shown for (c) 2^+ $(E^*=1.8$ MeV) resonance and (d) dipole $(E^*\leqslant 4.5$ MeV) excitations in the ^{6}He in elastic breakup reactions on ^{12}C at 240 MeV/nucleon collision energy. Solid, dashed, and dotted lines are for the differential cross sections of total, halo neutrons, and α-core nucleons, respectively.

$=\langle\Phi\|\Sigma_{i=1}^4 j_0(k\xi_i)\|\Phi\rangle$ is the nucleon matter density of the α particle, normalized at $k=0$ to the number of core nucleons.

The factor $\rho^{l0l}_{\alpha_{\rm c.m.}}$ in Eq. (48) gives contributions only to the normal parity $(l=j)$ excitations with transferred spin $s=0$ and cannot give contributions to excitations with spin $s=1$. It means that in the three-body cluster model the interactions with the α-core nucleons can excite the nucleus only to normal parity states without spin flip. The coordinate $\boldsymbol{r}_3$ of the α c.m. relative to O is proportional to the Jacobi coordinate $\boldsymbol{y}$, $\boldsymbol{r}_3=\beta\boldsymbol{y}$. The transition density $\rho^{lsj}_{\alpha_{\rm c.m.}}$ represents a recoil effect in the system. If the core mass m_3 goes to infinity $(\beta\to 0)$, the transition density operator becomes independent of internal coordinates and due to orthogonality of nuclear states with different energies, the core transition density is zero. To exemplify this, Fig. 3(a) shows the modulus of the real part of $\rho^{l0l}_{\alpha_{\rm c.m.}}(r)$ (dashed line) and $\rho^{l0l}_n(r)$ (solid line) transition densities $(l=j=2,s=0)$ to the $(KLSl_xl_y)=(22002)$ component of the continuum wave function at the 2^+ resonance peak energy $(E^*=1.8$ MeV), respectively. The recoil density is concentrated at small radii, while the halo neutron density has larger spatial extension and dominates in the outer region. If the core mass m_3 is increased, the proportionality coefficient β between the $\boldsymbol{r}_3$ and $\boldsymbol{y}$ coordinates becomes smaller and the recoil density $\rho^{l0l}_{\alpha_{\rm c.m.}}$ will be compressed to smaller radii.

The concentration of the recoil transition density at small radii means that in momentum space the recoil density will be concentrated at large momenta and we can expect an increasing core contribution to a reaction cross section with increasing transferred momenta. Figure 3(b) shows the transition densities in momentum space. The halo neutron density (solid line) is concentrated at low momenta. The recoil density (dashed line) has a wide extension in momentum space. The α-particle matter density $\rho_{mat}(k)$ [37] is shown by the dashed-dotted line. It cuts $\rho^{lsj}_{\alpha_{\rm c.m.}}(k)$ at large momenta and the transition density $\rho^{lsj}_{\alpha}(k)$ (dotted line) of α-core nucleons has a shape similar to that of a halo neutron but shifted to larger momenta.

Figure 3(c) shows the theoretical differential cross sections for excitation of the 2^+ resonance in inelastic scattering of ^{6}He on ^{12}C at collision energy 240 MeV/nucleon. The total differential cross section and separate contributions from interactions with halo and core nucleons are shown by solid, dashed, and dotted lines, respectively. The core cross section has a maximum at larger angles than that from the halo neutrons. The two contributions become equal at the upper end of the shown angular interval (at transferred momentum ~ 1 fm^{-1}). At larger momenta the core contribution dominates. This tendency shows that a large momentum is more easily transferred in scattering via the more massive α constituent. The total differential cross section for the 2^+ resonance shows a strong constructive interference between halo and core contributions.

Another example of interplay between core and halo nucleons is given in Fig. 3(d) where the angular distribution for dipole excitations with $E^*\leqslant 4.5$ MeV is shown [the notation is the same as in Fig. 3(c)]. The peak at forward angles is due to pure Coulomb excitations and it is completely determined by the α-core contribution. The second peak at larger angles is excited by the nuclear interaction. The core contribution is roughly twice that of the halo nucleons and shifted to larger angles. But now there is a destructive interference between the halo and core degrees of freedom. The total cross section is less than the individual contributions and shows a bump at larger angles. Hence, a correct treatment of translational invariance in light nuclei such as ^{6}He, intimately connected with recoil effects, is an important part of reaction dynamics and has to be taken into account in quantitative descriptions of nuclear reactions.

III. RESULTS AND DISCUSSION

A. Physical input to the calculations

Before a discussion of results the necessary details on the physical ingredients in the microscopic model of a two-neutron halo breakup have to be reemphasized. As follows from the formulas above, in the distorted-wave framework

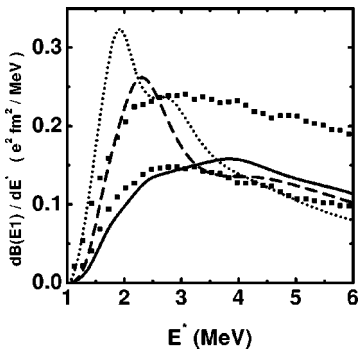

FIG. 4. Dipole strength distributions for ^{6}He. Dashed, dotted, and solid lines are for previous theoretical calculations from Refs. [10,11] and present work, respectively. Dark squares are experimentally derived boundaries from Ref. [12].

the reaction amplitude has three ingredients: (i) The structure of the target nucleus (matter density) and of the halo system (transition densities). (ii) The nucleon-nucleon effective interactions between projectile and target nucleons. (iii) The optical potentials for relative motion of projectile and target nuclei.

(i) The matter density distributions of ^{12}C and ^{208}Pb nuclei have the two-parameter Fermi form with parameters [38] chosen to reproduce the rms radius and surface thickness of density distributions.

To calculate transition densities for ^{6}He we employ the method of hyperspherical harmonics [10]. The quantitative calculations have been carried out with the GPT n-n potential and Kukulin's $n-\alpha$ potential[2] with even-odd splittings [39] for $K_{\max}=40$ (0^+),$K_{\max}=39$ (1^-) [10]. A polarization potential with inverse cubic dependence [10] was added in the ground-state calculation to reproduce the binding energy. The treatment of the Pauli principle followed in Ref. [40] has been extended, but will be discussed in a separate publication [41]. Our results, except for the dipole excitation (see below), do not depend essentially on this modification. The Feshbach reduction to active subspace was used, and in all partial states we have reduced the initial $K\sim 40$ hyperharmonic space (enough for practical convergence) to $K\sim 10$, which gives the same results as a strict calculation in the larger initial space. With this structure input, we calculated the soft dipole response function. The comparison with the experimental GSI data [12] is shown in Fig. 4 by the solid line. Monopole 0^+, dipole 1^-, and quadrupole 2^+ excitations in ^{6}He with energies from threshold up to 10 MeV, were considered.

(ii) The effective NN interaction V_{pt} defines the dynamics of the one-step reactions. At intermediate collision energies the impulse approximation is reasonable and has proven to be very successful. In this approximation the nucleon-nucleon t matrix describing a free NN scattering is used as an effective interaction. In the calculations we used the t-matrix parametrization by Love and Franey [42]. The contribution of an exchange knockout amplitude was taken into account in the pseudopotential approximation.

TABLE I. Theoretical (integrated over excitation energy $E^*\leqslant 10$ MeV) cross sections (mb) for inelastic excitation of ^{6}He at 240 MeV/nucleon on ^{208}Pb and ^{12}C targets. N (C) labels calculations with purely nuclear (Coulomb) forces. Experimental data [12] include cross sections up to $E^*\leqslant 12.3$ MeV.

	Total	Elas.	Inel.	0^+	1^-	2^+	2^+_{res}
^{208}Pb							
$N+C$	578	378	199	82	320	176	87
N	320	136	184	82	55	184	91
C	252	224	28	0	251	1	0.3
Expt. [12]	650 ± 110						14 ± 4
^{12}C							
$(N+C)$ [a]	25.5	14.6	11	3	7.6	15	7.9
N [a]	24.7	13.2	11.5	3	6.3	15.4	8.1
C [a]	1.6	1.5	0.1	0	1.6	0.02	0.01
$(N+C)$ [b]	31.4	16.9	14.5	6.1	9.9	15.3	8.1
Expt. [12]	30 ± 5						4 ± 0.8

[a][43].
[b][44] are the optical potentials used in the calculations.

(iii) Heavy ion elastic scattering defines the optical potentials needed for calculations of the distorted waves in the initial channel. Until now, there are no experimental data for elastic ^{6}He scattering from the ^{12}C and ^{208}Pb nuclei. Therefore, optical potentials for ^{12}C scattering on ^{12}C and ^{208}Pb targets at energy 200 MeV/nucleon [43] were used. (The radius parameters were scaled proportionally to the number of nucleons in ^{6}He.) For fragmentation on ^{12}C the calculations have also been done with the optical potential from work [44]. This optical potential describes the experimental data for ^{12}C-^{12}C elastic scattering in a large angular region at energy about 100 MeV/nucleon and has a shallow imaginary part. This energy is probably somewhat low but comparison of our results with different types of potential (''deep'' and ''shallow'') may give an estimation of ambiguity and check the sensitivity of breakup calculations to the optical potentials. Since the nuclear excitation energy is negligibly small in comparison with the collision energy, the optical potential in the final channel is taken to be the same as in the initial.

B. Inclusive excitation spectra

Table I gives total theoretical cross sections integrated over excitation energy up to 10 MeV for inelastic scattering of ^{6}He on ^{208}Pb and ^{12}C targets. Figures 5 and 6 show the corresponding spectra compared with experimental data [12]. The calculations correctly describe absolute values and spectral shapes for both reactions, in spite of their different reaction mechanisms. Still theory underestimates the total cross sections somewhat, caused by insufficient contributions at higher E^*. In this respect the calculations can be improved by inclusion of excitations with higher multipolarities [15], currently not taken into account.

[2]In comparison with our earlier paper [17], we have used an improved version of the $n-\alpha$ potential and an improved computational technique. Hence, the results differ numerically slightly from previous work, but the conclusions are not changed.

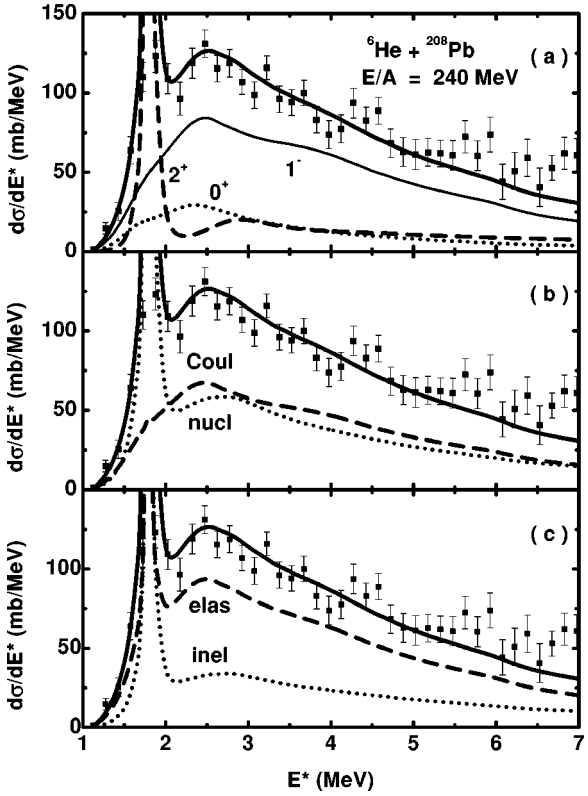

FIG. 5. Comparison of the theoretical ^{6}He excitation spectrum (thick solid line) for ^{6}He+ ^{208}Pb breakup at 240 MeV/nucleon with experimental data [12]. (a) The thin solid, dashed, and dotted lines show the dipole 1^-, quadrupole 2^+, and monopole 0^+ contributions. (b) Dashed (dotted) lines show calculations with only nuclear (Coulomb) interactions. (c) Dashed (dotted) lines are contributions from elastic (inelastic) fragmentation.

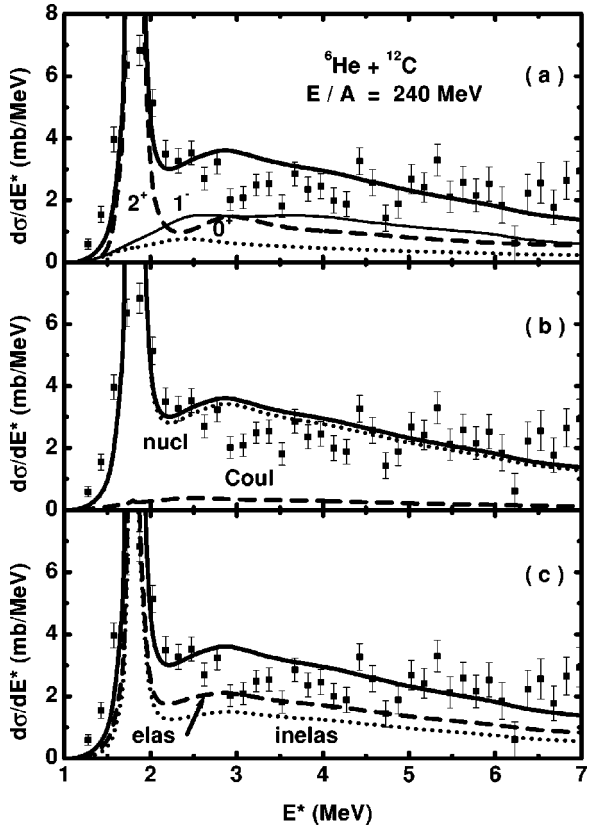

FIG. 6. The same as in Fig. 5 but for the ^{6}He+ ^{12}C reaction.

The contributions [Fig. 5(a)] to inclusive spectra on lead target from different multipole excitations in ^{6}He display a small monopole contribution, while the dipole dominates and the well-known three-body 2^+ resonance at 1.8 MeV is strongly excited (total cross section ~90 mb). Since the calculated 2^+ resonance width (~60 keV) is less than the experimental (~113 keV) and no energy averaging over experimental resolution performed, the theoretical peak cross section exceeds the experimental one. The steep cross-section increase at threshold is completely due to dipole excitations. Figure 5(b) shows the cross sections for calculations with only Coulomb or nuclear interaction. Coulomb dissociation dominates, but cannot alone describe the absolute values of experimental data. Applying the semiclassical method to our dipole strength function gives ~355 mb for a cutoff minimum impact parameter of 9.5 fm. Quantum calculations when only the Coulomb part of the optical potentials is present gave ~330 mb for the dipole elastic cross section. The excitation of the 2^+ resonance is connected mainly with the nuclear interaction. The Coulomb and nuclear dissociations have a different dependence on excitation energy E^*. The Coulomb cross section dominates at smaller E^* but falls rapidly with increasing energy. The nuclear part has a weak dependence on E^* and decreases with energy rather slowly. As a result, the two contributions become equal around $E^* \sim 7$ MeV. The cross section contributions from elastic and inelastic fragmentation are shown in Fig. 5(c). Although the elastic fragmentation dominates the low-energy part of the spectrum, for a quantitative description both contributions have to be taken into account simultaneously. Near the threshold, the total cross section coincides with the elastic. Elastic and inelastic fragmentations give approximately equal contribution to the 2^+ resonance. The dependence on E^* is different for the two processes. The elastic fragmentation cross section decreases rapidly with energy while the inelastic stays rather flat. In total, σ_{in} on ^{208}Pb contributes about 30% of the total cross section for $E^* \leqslant 10$ MeV.

Figure 6 shows comparisons of theoretical calculations, (using optical potential [43]) with experimental data [12] for ^{6}He+ ^{12}C at 240 MeV/nucleon. The peak, the most pronounced feature in the spectrum, is due to excitation of the 2^+ resonance [Fig. 6(a)] with total cross section ~8 mb. Above the resonance, in the flat part of spectrum, approximately half of the cross section is due to dipole, a third is quadrupole, and the rest is monopole excitations. On carbon target the inclusive excitation spectrum is completely defined by nuclear interaction [Fig. 6(b)] and the contributions from elastic and inelastic fragmentations are approximately equal [Fig. 6(c)]. The excitation energy dependence is weak, but still the cross section for elastic fragmentation shows a tendency of decreasing fastest when E^* becomes larger.

As experiments show, the low-lying ^{6}He inelastic spectra for reactions on ^{12}C and ^{208}Pb targets have different shapes.

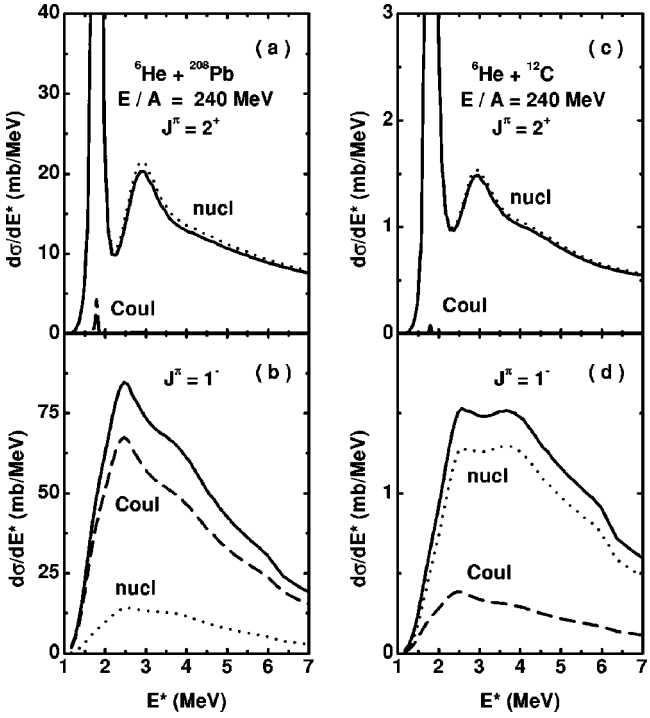

FIG. 7. Quadrupole (a) and dipole (b) excitations of the ^{6}He on ^{208}Pb, and quadrupole (c) and dipole (d) excitations on ^{12}C. Dashed (dotted) lines show calculations with only Coulomb (nuclear) interactions.

This difference has a dynamical origin and can be explained by interplay of short-range nuclear and long-range Coulomb interactions. The reaction form factor, due to attractive nuclear forces, has a finite extension in coordinate space. Coulomb repulsion reduces the nuclear form factor at small radii and produces a Coulomb tail (45) at large. The rate of the tail falloff is defined by the transition multipolarity. The monopole should decrease most slowly, but due to orthogonality between the ground and excited 0^+ states of ^{6}He, the monopole form factor is zero at large distances. Hence, the dipole form factor has the longest extension in space and dipole excitations are the most sensitive to the strength of Coulomb interaction. Both space regions, internal and external, cause a breakup reaction. In breakup on ^{12}C, the contribution from the internal region dominates while for the ^{208}Pb case, due to strong Coulomb interaction, the reverse is true. Figure 7 shows by solid lines the quadrupole [Figs. 7(a) and 7(c)] and dipole [Figs. 7(b) and 7(d)] excitations of the ^{6}He for reaction on the ^{12}C and ^{208}Pb targets. The dashed and dotted lines are for excitations caused only by Coulomb or nuclear interactions, respectively. For quadrupole transitions [Figs. 7(a) and 7(c)] the Coulomb interaction is not important. For both targets they are excited mainly by nuclear forces (dotted lines) and the cross section is roughly increased by one order of magnitude going from light to heavy targets. For dipole excitations [Figs. 7(b) and 7(d)] the picture is qualitatively different. The nuclear excitations (dotted lines) are more than two times bigger than Coulomb in breakup on ^{12}C and its cross section is roughly increased by one order of magnitude in the reaction on ^{208}Pb. But dipole

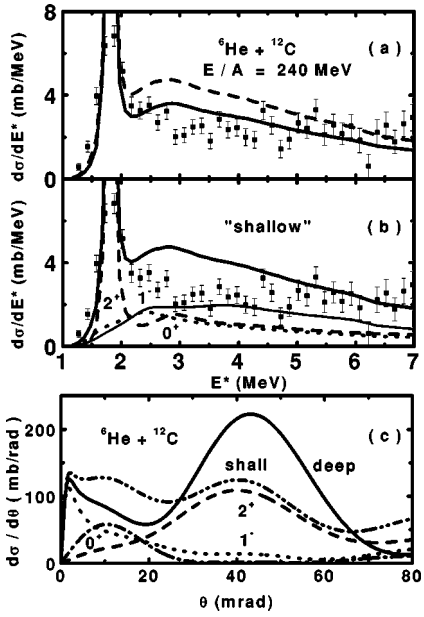

FIG. 8. (a) Comparison of the theoretical ^{6}He excitation spectrum for ^{6}He+ ^{12}C breakup at 240 MeV/nucleon for calculations with the ''shallow'' (solid line) and ''deep'' (dashed line) optical potentials. (b) The thin solid, dashed, and dotted lines show the dipole 1^-, quadrupole 2^+, and monopole 0^+ contributions for calculations with the ''shallow'' optical potential. (c) Differential cross sections for ^{6}He inelastic scattering at 240 MeV/nucleon in ^{12}C target for region of excitation energies $E^* \leqslant 4.5$ MeV. The solid, dashed, dotted, and dash-dotted lines are for the total, 2^+, 1^-, and 0^+ transitions, respectively. The double-dotted dashed line is the total cross section for ''deep'' optical potential.

cross sections due to Coulomb forces (dashed lines) are increased by more than two orders of magnitude going from carbon to lead targets. This factor is similar to the square of the ratio of target charges and is expected for pure Coulomb excitations. When both interactions are present, the picture becomes more complex: There is a destructive interference in the internal region and Coulomb excitation in the outer. Therefore, explicit calculations are needed to get a quantitative result.

In the calculations discussed above, we used the optical potentials [43] fitted to describe the ^{12}C elastic scattering at 200 MeV/nucleon on the carbon and lead targets with radius parameter scaled to the ^{6}He size. Therefore, it is reasonable to estimate the uncertainty of the calculations and check the sensitivity of the results to potential variations. As an alternative, we choose the optical potential from work [44] fitted to elastic data on ^{12}C+ ^{12}C scattering in a large angular interval at energy $\sim$100 MeV/nucleon. This energy is lower than ours but the potential has a ''shallow'' imaginary part and is an example of another class of optical potentials. With radius parameter scaled to ^{6}He, this potential may give a reasonable variation of the optical potential. It is of special interest to estimate the influence on inelastic fragmentation that is formally proportional to the potential imaginary part [see Eq. (11)]. Figure 8(a) compares the calculations of the inelastic spectrum for ''deep'' (dashed line) and ''shallow'' (solid line) potentials. The calculations with the shallow potential have a similar spectral shape but somewhat larger

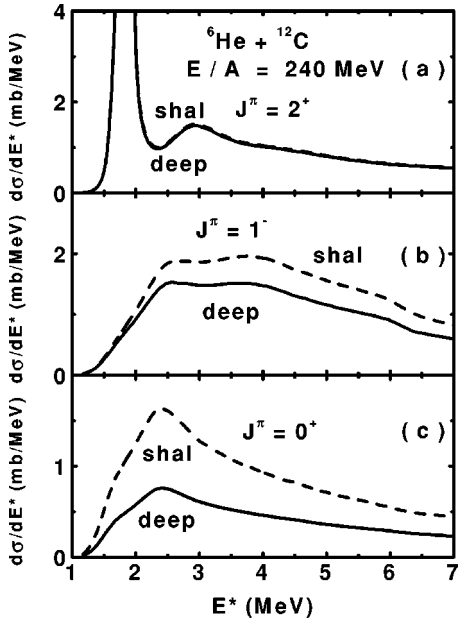

FIG. 9. Comparison of different multipole contributions for calculations with the ''deep'' (solid line) and ''shallow'' (dashed line) optical potentials. The quadrupole, dipole, and monopole are shown in (a), (b), and (c), respectively.

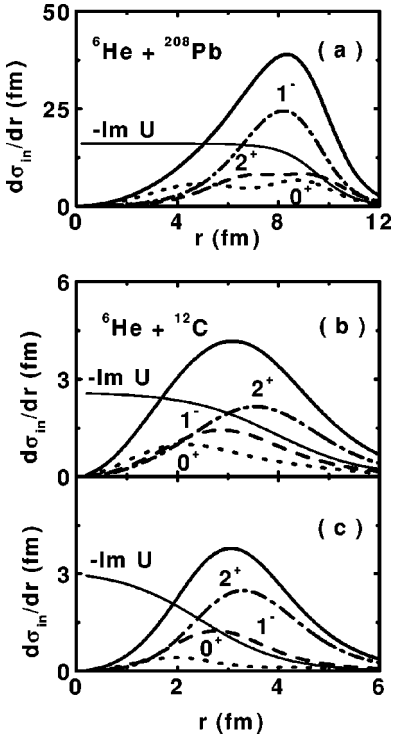

FIG. 10. The radial distributions of the inelastic ^{6}He breakup at 240 MeV/nucleon (a) on the ^{208}Pb target, (b) and (c) on the ^{12}C target calculated for the ''shallow'' and ''deep'' optical potentials. The thick solid, dashed, dash-dotted, and dotted lines show the total, dipole, quadrupole, and monopole contributions, respectively. The thin solid line shows the arbitrarily scaled imaginary part of optical potential.

values of absolute cross sections. The total cross section from threshold up to 10 MeV excitation energy is increased by 20%. Figure 8(b) shows for the shallow potential the decomposition of the inelastic spectrum on contributions from different multipole excitations (thin solid, dashed, and dotted lines for 1^-, 2^+, and 0^+, respectively). The most remarkable observation is the increase of monopole cross sections. To demonstrate better these changes, Fig. 9 shows the comparison of calculations with ''deep'' (solid lines) and ''shallow'' (dashed lines) potentials for different multipole excitations. It has been seen from Fig. 9(a) that quadrupole transitions have only minor changes. Dipole cross sections [Fig. 9(b)] are increased by 30%. The most significant increase [Fig. 9(c)] by more than two times is that of the monopole excitations. It is clearly demonstrated that using the shallow or transparent potential, influences most strongly the excitations that are concentrated more deeply inside the nucleus. The contributions from elastic and inelastic fragmentation for shallow potentials are increased similarly, inelastic slightly more then elastic.

It is useful to get a more detailed insight into the inelastic fragmentation, especially the spatial distribution for inelastic fragmentation cross sections as it is defined by Eq. (11). Figure 10 shows the radial distributions of total inelastic fragmentation cross sections for reaction on ^{208}Pb [Fig. 10(a)] and on ^{12}C for calculations with shallow [Fig. 10(b)] and deep [Fig. 10(c)] optical potentials. The thick solid, dashed, dashed-dotted, and dotted lines denote the total, 1^-, 2^+, and 0^+ cross sections, respectively. Thin solid lines denote the imaginary parts of corresponding optical potentials, scaled arbitrarily. The curves show that inelastic fragmentation (thin solid lines) is concentrated in the surface region. It is suppressed in the internal region since the significant partial waves that define the Green's function behavior at small radii, are suppressed due to absorption. At large radii, the exponential decrease of the optical potential imaginary part is responsible for suppression. This behavior clearly demonstrates the peripheral nature of the inelastic fragmentation reaction. Physically, the suppression in the internal region singles out the reactions that do not destroy the core. The suppression at large radii means that nuclei have to be close enough to excite each other.

An additional observation is related to the radial distributions of different multipole cross sections. The higher the multipolarity, the more an excitation is shifted to the surface. The monopole (dotted lines) has a volume character, the dipole (dashed lines) is concentrated on the surface, and the quadrupole (dashed-dotted lines) is shifted even further from the center. The radial distributions for the shallow potential [Fig. 10(b)] are broader than those for the deep one [Fig. 10(c)]. A transparent potential more strongly underlines the partial waves with low values of orbital momenta than an absorptive one. Therefore, contributions from the internal space play a bigger role in the reaction in comparison with the case of strong absorption. It qualitatively explains the doubling of the monopole and minor influence on the quadrupole contributions in calculations with deep and shallow potentials. Practically, there are two competitive factors acting in different directions. One is that an inelastic fragmentation cross section (11) is proportional to the absolute value

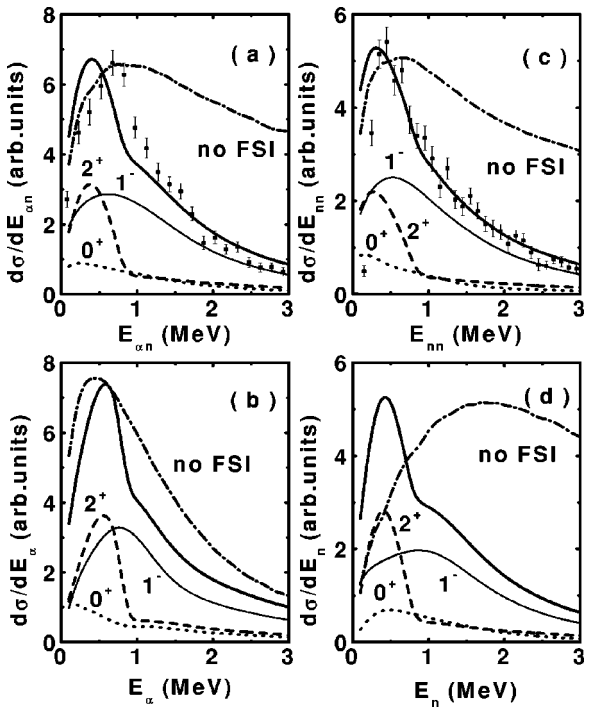

FIG. 11. Top: Comparison of the theoretical spectra of the relative energy between the α particle and a halo neutron (a), and between two halo neutrons (c), for ^{6}He+ ^{208}Pb breakup at 240 MeV/nucleon with experimental data [12]. Bottom: Energy spectra of α particle (b), and of a halo neutron (d), in the projectile rest frame. The thick solid, thin solid, dashed, and dotted lines show the total, dipole 1^{-}, quadrupole 2^{+}, and monopole 0^{+} contributions, respectively. The dash-dotted lines correspond to calculations of total spectra without final-state interactions.

of imaginary potential part. The second is that a large absorption strongly suppresses the contributions from the internal region and, hence, decreases the cross section. In our case the second factor is more significant.

C. Fragment energy distributions

Figure 11 shows the different fragment energy spectra for ^{6}He breakup on ^{208}Pb target. The α-neutron and neutron-neutron relative energy distributions are compared with experimental data [12] in Figs. 11(a) and 11(c). The α-particle and the halo neutron energy spectra in the projectile rest frame are shown in Figs. 11(b) and 11(d). The thick solid, thin solid, dashed, and dotted lines show the total, dipole 1^{-}, quadrupole 2^{+}, and monopole 0^{+} contributions, respectively. The theoretical two-body energy correlations [Figs. 11(a) and 11(c)] correctly reproduce the falloff of the cross sections with increasing relative fragment energy, but at small energies there are some deviations from measured data. For a fair comparison with experiment the theoretical calculations have to be folded with instrumental response in order to correct for efficiency and solid-angle acceptance of the fragment detectors. Since these experimental distortions are not included in the calculations, it is premature to draw definite conclusions from this comparison. Decays from the dipole excitations dominate the energy spectra and define the slope at large energies. Decays from quadrupole states (from the three-body 2^{+} resonance) are important at small energies. The neutron-neutron spectrum [Fig. 11(c)] from the 2^{+} resonance has a peak close to the threshold revealing the strong nucleon-nucleon correlations. The shapes of the 2^{+} α-particle and neutron spectra [Figs. 11(b) and 11(d), dashed lines] are qualitatively similar to the shapes that were measured from decay of the 2^{+} resonance populated in the ^{7}Li$(d,^{3}$He$)^{6}$He$(J^{\pi}=2^{+},E^{*}=1.8$ MeV) reactions [45,46]. It is interesting to note that the shape of the total α-particle spectrum [Fig. 11(b), thick solid line] coincides perfectly with experimental data for neutron-α correlations [Fig. 11(a)]. To demonstrate the importance of final-state interactions, the dash-dotted lines in Fig. 11 show the calculations when mutual interactions between the projectile fragments in the exit channel were neglected (the fragment relative motion are described by three-body plane waves), while the halo ground-state wave function keeps a complex correlated structure. We see that only the spectrum of the single heavy fragment [Fig. 11(b)] has a shape qualitatively similar to the full calculation (still the width of the peak is essentially broader) while all other spectra differ markedly.

D. Fragment momentum distributions

Recently [16] we demonstrated within our microscopic approach that in diffractive (elastic) breakup of Borromean halo nuclei on proton target, the correlated continuum excitations play a crucial role in fragment momentum distributions. Now, similar properties are revealed in ^{6}He fragmentation on complex nuclei when processes of elastic and inelastic fragmentation take place.

Figure 12 shows α-particle longitudinal momentum distributions for ^{6}He breakup on ^{12}C target at 240 MeV/nucleon. In Fig. 12(a) the thick solid line shows the total distribution that includes contributions from the continuum excitations with energy $E_{\kappa}<10$ MeV. To clarify the nature of the momentum distributions, the contributions from three different intervals of the ^{6}He continuum (see caption of Fig. 12) are also shown. The well-known 2^{+} resonance at $E_{\kappa}=0.83$ MeV, which dominates in ^{6}He energy spectra [12], determines the contribution from the first interval. The second interval contains excitations of different soft modes, while the third corresponds to the highest excitation energies taken into account in our model. We see that a narrow width of a momentum distribution is due to decays of excitations near the breakup threshold (from the first and second intervals). The decays from the highest excitation energies (the third interval) give a broad distribution and define the wings of the total distribution (at a fixed excitation energy the magnitude of a fragment momentum is restricted by allowed phase space). Since momentum distributions are highly integrated observables, their dependence on the exact location of the soft modes and higher excitations is not strong.

Figure 12(b) shows the partial content, i.e., contributions from continuum states with different J_{f}^{π}. Since amplitudes for different states interfere with each other, an estimate of the partial contributions was carried out by incoherently adding the cross sections for all J_{f}^{π}. The difference between this (dash-dotted) line and the one corresponding to the complete

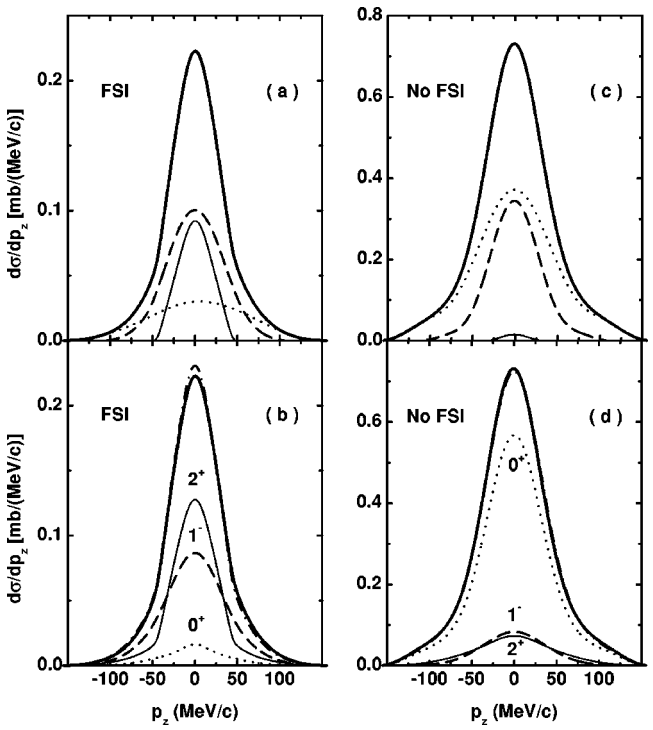

FIG. 12. The calculated longitudinal α-particle momentum distributions in ^{6}He breakup on ^{12}C target at 240 MeV/nucleon: (a) and (b) include FSI, while (c) and (d) are without FSI. The thick solid line shows the total momentum distribution. For (a) and (c), the thin solid, dashed, and dotted lines correspond to the contributions from the ^{6}He continuum for excitation energy intervals $0<E_{\kappa}<1$ MeV, $1<E_{\kappa}<5$ MeV, and $5<E_{\kappa}<10$ MeV, respectively (E_{κ} measured from the three-body threshold $E_{thresh}=0.97$ MeV). For (b) and (d) the dashed-dotted line shows total distribution without interference between excitations with different J_f^{π}; the thin solid, dashed, and dotted lines show contributions from decay of the 2^+, 1^-, and 0^+ excitations, respectively.

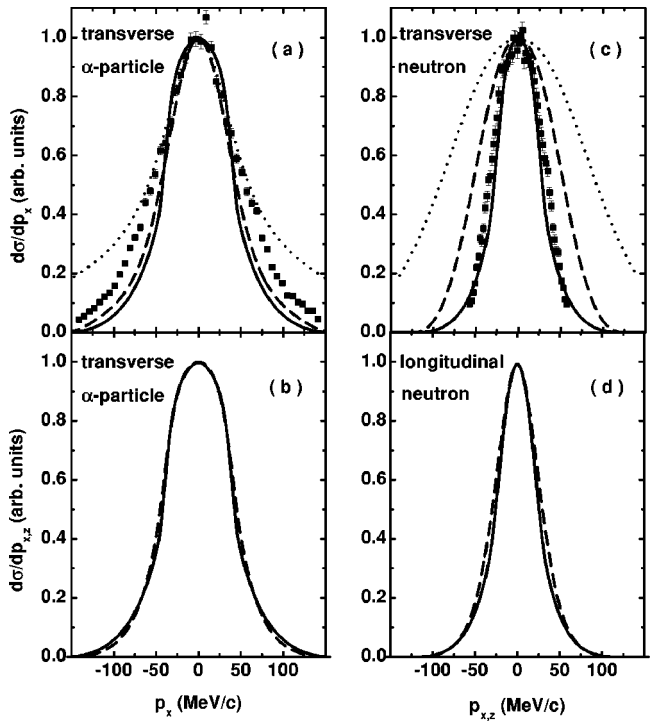

FIG. 13. Momentum distributions for ^{6}He breakup at 240 MeV/nucleon, normalized to unity at zero momentum. (a) and (c) show transverse α and halo neutron distributions on ^{12}C target, respectively. The solid (dashed) line shows total momentum distribution with (without) final-state interaction. The dotted line is the distribution from the Serber model. The experimental data (black squares) from [19] correspond to the coincidences between an α particle and a neutron. (b) and (d) show α-particle transverse and halo neutron longitudinal momentum distributions. The solid (dashed) line corresponds to the reaction on ^{12}C (^{208}Pb) target.

calculation (thick solid line), gives an estimate of the importance of such interference. In our case, the interference is small. The shape of the longitudinal distribution is slightly asymmetrical [asymmetry is seen in high momentum tails in Fig. 12(a)], which supports this statement. The decay from 2^+ is the largest and gives the narrowest part of the distributions, the 1^- is the second in importance, and the 0^+ gives a small contribution. Hence, the structure of the continuum determines the essential features of momentum distributions.

In Figs. 12(c) and 12(d), the situation with no FSI is shown, i.e., the continuum ^{6}He wave functions were described by three-body plane waves, but correlations in the ground state were kept the same. Large differences are seen when neglecting FSI: the 2^+ resonance disappears, and there is practically no contribution from the low-energy region. The contribution from the highest excitation energies is the largest. The width of the distributions is correspondingly increased, and the partial content is strongly changed. The contribution from the 0^+ dominates the momentum distribution while the role of the 2^+ and 1^- excitations become essentially smaller. Monopole wave functions for continuum excitations must be orthogonal to the ground state since they have the same quantum numbers and correspond to different energy eigenvalues of the projectile Hamiltonian. Neglecting the FSI leads to violation of this important requirement. Thus, the final-state interaction is decisive: It defines the structure of the continuum excitations that directly influences the width of the momentum distributions.

The calculated core and neutron transverse momentum distributions in various approximations and normalized to unity at zero momentum, are compared with experimental data [19] for ^{6}He fragmentation on the ^{12}C target in Figs. 13(a) and Fig. 13(b). The solid (dashed) lines correspond to calculations with (without) final-state interactions, and the dotted line shows the transverse distributions from the Serber model [47]. The experimental data (black squares) [19] correspond to the coincidences between an α particle and a neutron. The Serber model does not simultaneously describe the core and neutron momentum distributions. For the core, it overestimates the distribution wings, which demands cutting the contribution for high momentum. For the neutron, it gives a significantly broader distribution. Calculations (dashed lines) that take into account the reaction mechanism and the correlations in the ground state, but neglect FSI, are also insufficient and overestimate the width of the neutron distribution. Because of the FSI, a redistribution of transition

strength over continuum excitation energy occurs, the low-energy part being enhanced. As a result, the momentum distributions become narrower than without FSI. Since the final-state interaction most strongly influences the motion of the light fragments, the shape of the neutron distribution changes more strongly than for the α particle. Finally, the full calculations with FSI (solid lines) are slightly narrower than the experimental data for both fragment distributions. The reason is that the theoretical calculations include only the low-energy part ($E_\kappa < 10$ MeV) ^{6}He excitation spectrum (with undestroyed α particle) while the experimental data contain also fragments from higher excitations since the ^{6}He excitation energy cannot be defined from a single α-neutron coincidence. The fragments from high-energy excitations have a flat, broad momentum distribution and taking their contribution into account in theoretical calculations will improve the agreement with experimental data. The α-particle transverse and neutron longitudinal momentum distributions for ^{6}He breakup on ^{12}C (solid line) and ^{208}Pb (dashed line) targets are compared in Figs. 13(b) and 13(d), respectively. We see that the shapes of the momentum distributions for both reactions are rather similar in spite of differences in reaction mechanism.

E. Differential angular cross sections

In the approach we have developed, we can, as was mentioned above, only calculate a differential angular cross section $d^2\sigma/d\hat{\boldsymbol{k}}_f$ for processes of elastic ^{6}He fragmentation, i.e., when the target does not get excited in the reaction. In kinematically complete experiments, it is possible to reconstruct the ^{6}He recoil momentum as a sum of the momenta of all fragments $\boldsymbol{k}_{n_1}+\boldsymbol{k}_{n_2}+\boldsymbol{k}_\alpha$ and get the angular distribution of the ^{6}He c.m. motion at fixed excitation energy. Since it is unknown how the energy transferred to the target is distributed between the c.m. motion and the internal excitation of the target, the experimental data contain the events for both processes: elastic and inelastic breakup. Therefore, a quantitative comparison of theoretical angular distributions with experimental data is less certain.

Figure 14 shows the angular distributions $d\sigma/d\theta$ for inelastic scattering of ^{6}He in carbon [Figs. 14(a) and 14(b)] and lead [Fig. 14(c)] targets at 240 MeV/nucleon. Experimental data are from Ref. [20]. Figures 14(a) and 14(c) contain the events with ^{6}He excitation energy $\leqslant 4.5$ MeV, the Fig. 14(b) is for a more narrow range of $E^* \leqslant 2.5$ MeV to underline the role of the 2^+ resonance. The solid, dashed, dotted, and dashed-dotted lines correspond to the theoretical calculations of the total, quadrupole, dipole, and monopole contributions of elastic fragmentation leading to the ^{6}He excitations lying in the energy ranges. For breakup on ^{12}C target [Figs. 14(a) and 14(b)] the experimental data and theoretical calculations give similar shapes with a narrow peak at extremely forward angles and broader bump at $\theta \sim 40$ mrad. The nature of the broad bump is explained by the excitation of the 2^+ resonance [Fig. 14(b)] that dominates in the low-lying part of the ^{6}He inelastic spectrum. At higher E^*, the dipole excitations are also important in addition to quadrupole transitions. They have their maxima in the angular distribution at angles slightly smaller than those of quadrupole and, as a result, the total angular distribution becomes broader [Fig. 14(a)] than it is for pure quadrupole excitations. The nature of the small-angle peak in the theoretical calculations is completely due to dipole excitations. Furthermore, if the attractive nuclear part from a projectile-target NN interaction V_{pt} is switched off, the forward-angle peak keeps its position and absolute magnitude [thin solid line in Fig. 14(a)] while the peak at larger angles (nearly quadrupole) disappears. Hence, we conclude that pure Coulomb interaction is responsible for the forward-angle peak. This is a signal of long-ranged breakup of the halo nucleus on a light target that, due to the weakness of Coulomb forces in such systems, is clearly separated from nuclear breakup.

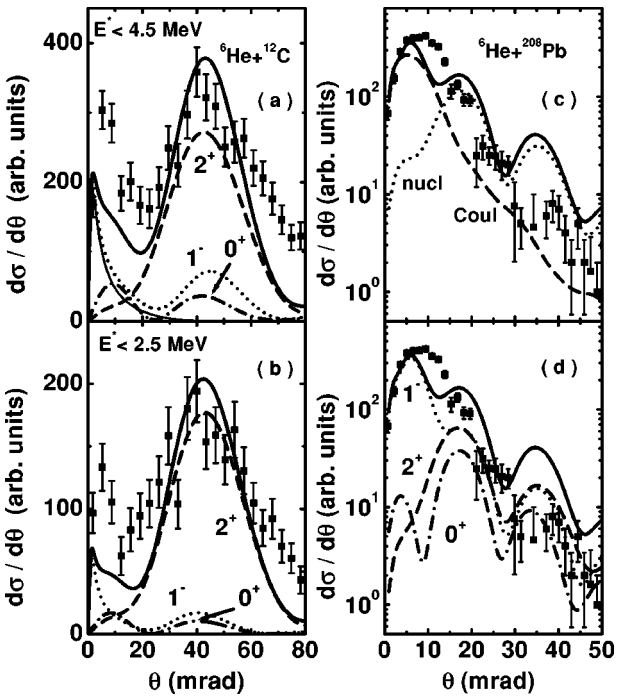

FIG. 14. Differential cross sections for ^{6}He inelastic scattering at 240 MeV/nucleon in (a) ^{12}C target for ^{6}He excitation energies $E^* \leqslant 4.5$ MeV; (b) ^{12}C target for excitation energies $E^* \leqslant 2.5$ MeV; (c), (d) ^{208}Pb target for region of excitation energies $E^* \leqslant 4.5$ MeV. The solid, dashed, dotted, and dash-dotted lines in (a), (b), and (d) are for the total, 2^+, 1^-, and 0^+ transitions, respectively. The thin solid line in (a) shows calculation of differential distribution in the case where only Coulomb forces are present in the projectile-target NN interaction V_{pt}. In (c), the dashed, dotted and solid lines correspond to calculations where the projectile-target NN interaction V_{pt} includes only Coulomb or nuclear forces and both together, respectively. The experimental data (black squares) are from Ref. [20].

The angular position of the very forward peak is rather stable in theoretical calculations. The quantal, semiclassical, or simply plane-wave Born estimations (which can be used since the Sommerfeld parameter η that characterizes the strength of Coulomb interactions is small, $\eta \sim 0.1$)—all give a peak position at angles of about 1 mrad. The experimental data indicate a peak at larger angles. The effects of distortions due to finite acceptance and efficiency of fragment de-

tection have to be applied to the theoretical calculations for a fair comparison with experimental data. The monopole excitations play a smaller role in the low-lying transitions since the monopole wave functions are orthogonal to the ground state having the same quantum numbers. But they have a maximum in angular distributions just at the place where the pure Coulomb dipole is significantly decreased, while the quadrupole is not yet enhanced and have to be taken into account in quantitative analysis of angular distributions.

Figure 8(c) demonstrates the sensitivity of angular distributions to the optical potentials used for description of the relative motion of the colliding nuclei. The first peak arising from Coulomb excitation does not show sensitivity while the second (mainly from nuclear interactions) is strongly decreased for a shallow potential. In this case in the angular region of the second bump, the quadrupole excitations are weaker, while the dipole and monopole show smooth falling behavior. Therefore, the description of an angular distribution due to nuclear interactions demands knowledge of optical potentials for which the elastic scattering data are required.

Figures 14(c) and 14(d) show differential distributions of ^{6}He breakup on the ^{208}Pb target. Coulomb forces are strong and predominantly excite the dipole transitions. The shape of angular distributions is rather smooth for a pure Coulomb interaction [dashed line in Fig. 14(c)]. But nuclear interactions are important since the interference with Coulomb produces irregularities in angular distributions. The strength of interference shows some sensitivity to the optical potential.

F. Angular distributions

For three-particle breakup of Borromean nuclei, a variety of different angular distributions can be studied. A detailed discussion of their properties will be given elsewhere. Here we give only one example—angular distributions of the α particle with respect to the beam direction for ^{6}He fragmentation on ^{12}C and we try to illuminate the main features of such distributions. Figure 15(a) shows the total distribution and separate contributions from the dipole, quadrupole, and monopole excitations. The α decay from the states in ^{6}He for $E^{*} \leqslant 10$ MeV were taken into account. The decay from monopole states is isotropic while that from the states with nonzero angular momentum shows anisotropy with increased probability to fly in the plane perpendicular to the beam direction. Figures 15(b), 15(c), and 15(d) show the α-particle angular distributions from elastic and inelastic breakup for different multipole excitations. We see that angular distributions from elastic and inelastic breakup are qualitatively different. Only the elastic breakup from states with nonzero total momenta shows an angular anisotropy while in inelastic fragmentation the α particles have no preferable direction. The formal reason is that the optical potential used for calculations of inelastic fragmentation in Eq. (36) is spherically symmetric. For nonzero values of L in Eq. (41), which describe the deviation from angular isotropy, the product of two inelastic amplitudes $\tilde{T}^{l_j,l_p,\delta}_{l_b,l_a}(R,k_f,k_i,\kappa)$ with different angular momenta l_a has radial oscillations. An integration over R decreases the terms with $L \neq 0$ and, finally, the angular distributions are flat.

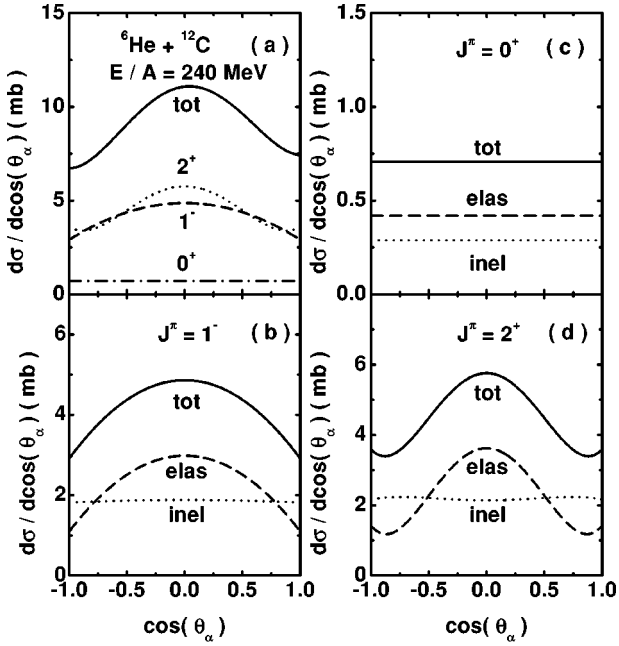

FIG. 15. Angular distribution calculations for the α fragment with respect to the beam direction, in the projectile rest frame for ^{6}He breakup on the ^{12}C target. (a) The solid, dashed, dotted, and dashed-dotted lines show the total, dipole, quadrupole, and monopole contributions, respectively. In (b), (c), and (d), the angular distributions for dipole, monopole, and quadrupole excitations are given separately. The solid, dashed, and dotted lines show the total, elastic, and inelastic contributions, respectively.

Figure 16 shows the same distributions as shown in Fig. 15 but for calculations without final-state interactions. The total angular distribution [Fig. 16(a)] is flatter in comparison with calculations with FSI. Comparisons of contributions for

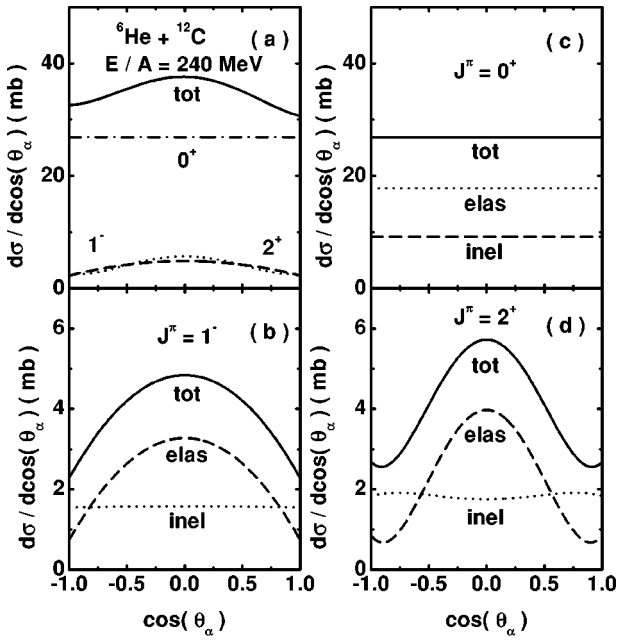

FIG. 16. The same as in Fig. 15 but without final-state interactions.

different multipole excitations [Figs. 16(b)–16(d)] with corresponding distributions in Figs. 15(b)–15(d) show that the dipole and quadrupole distributions are similar in shape and in absolute magnitude while the isotropic monopole is increased about 30 times in calculations without FSI. This again demonstrates the importance of the orthogonality between excited- and ground-state wave functions for monopole excitations lost in calculations without FSI.

IV. CONCLUSIONS

The characteristics of halo phenomena in light Borromean nuclei are present in properties of both bound and continuum states near the three-body breakup threshold. These states are also coupled by the ways we learn about halo phenomena; the nuclear reaction mechanism intertwines bound and excited states and reveals the peculiarities of halo structure via transitions to low-lying halo excited states that subsequently decay into fragments. These events can be studied by a hierarchy of observables in kinematically complete experiments. Such experiments allow sophisticated analyses of the data and give a possibility to reconstruct projectile excitation spectra and different correlations between fragments. In the quantitative theoretical analysis of such experiments, the final-state interactions between all halo fragments have to be taken into account. Due to the small relative fragment velocities at low halo-excitation energies, no interaction can be neglected. At these conditions, the no-FSI approximation, and even the spectator model, are invalid.

For definite physical conditions, simplification of the reaction mechanism makes it possible to develop a viable approach. At intermediate energies, the one-step reaction mechanism dominates and the distorted-wave impulse approximation (DWIA) can be applied. These approaches contain, as a main part, the microscopic three-body structure of the ground state and the exact three-body continuum [15]. This enables us to study, in principle, the internal halo structure via all possible fragment correlations.

We have extended our microscopic four-body DWIA theory for two-neutron halo breakup reactions to account for both elastic and inelastic breakups leading to low-lying halo excitations. Within this approach, the Coulomb and nuclear dissociations are included in a consistent way that also accounts for Coulomb-nuclear interference. The importance of a correct treatment of recoil effects in the reaction dynamics of the light breakup projectile has been demonstrated. The method of hyperspherical harmonics is used for a consistent description of genuine features of the halo bound-state and the final-state interactions between all halo fragments.

Our four-body DWIA theory can be applied to kinematically analyze complete experiments, which allow reconstruction of the halo excitation spectrum, and single out the events carrying the most valuable information on correlations specific to two-neutron halo systems.

The method was used to analyze recent experimental data [12,20] on ^{6}He fragmentation at 240 MeV/nucleon on ^{12}C and ^{208}Pb targets. In addition to a good simultaneous description of absolute cross sections and excitation spectra for both reactions, new insight into the interplay of reaction mechanisms and correlated continuum structure was obtained. It was shown that in breakup of Borromean nuclei, a fragment momentum distribution has a symmetrical shape for transverse while it may be asymmetrical for the longitudinal distribution. A number of other energy and angular correlations between halo fragments were calculated within the same dynamical picture. The important role found for inelastic fragmentation, i.e., inclusion of target excitations and Coulomb-nuclear interference, is consistent with experimental data. To reduce the uncertainties in the theoretical calculations, experimental data for elastic scattering of halo nuclei are needed, allowing us to more precisely define the reaction dynamics. Application of the approach to other Borromean nuclei is in progress.

ACKNOWLEDGMENTS

This work was done under financial support from the Bergen member of the RNBT Collaboration and the BCPL project. B.D. and S.E. are thankful to the University of Bergen for hospitality. B.D. acknowledges support from RFBR Grant No. 99-02-17610. The authors are grateful to Professor M. V. Zhukov for useful discussions.

[1] I. Tanihata, J. Phys. G **22**, 157 (1996).
[2] R. Serber, Phys. Rev. **72**, 1008 (1947).
[3] F. Barranco, E. Vigezzi, and R.A. Broglia, Z. Phys. A **356**, 45 (1996).
[4] M.V. Zhukov, L.V. Chulkov, D.V. Fedorov, B.V. Danilin, J.M. Bang, J.S. Vaagen, and I.J. Thompson, J. Phys. G **20**, 201 (1994).
[5] A.A. Korsheninnikov and T. Kobayashi, Nucl. Phys. **A567**, 97 (1994).
[6] Y. Suzuki, T. Kido, Y. Ogawa, K. Yabana, and D. Baye, Nucl. Phys. **A567**, 957 (1994).
[7] E. Garrido, D.V. Fedorov, and A.S. Jensen, Nucl. Phys. **A617**, 153 (1997).
[8] G.F. Bertsch, K. Hencken, and H. Esbensen, Phys. Rev. C **57**, 1366 (1998).
[9] J.A. Tostevin, J. Phys. G **25**, 735 (1999).
[10] B.V. Danilin, I.J. Thompson, M.V. Zhukov, and J.S. Vaagen, Nucl. Phys. **A632**, 383 (1998).
[11] A. Cobis, D. Fedorov, and A. Jensen, Phys. Rev. Lett. **79**, 2411 (1997).
[12] T. Aumann *et al.*, Phys. Rev. C **59**, 1252 (1999).
[13] J.S. Al-Khalili, I.J. Thompson, and J.A. Tostevin, Nucl. Phys. **A581**, 331 (1995).
[14] B.V. Danilin, M.V. Zhukov, S.N. Ershov, F.A. Gareev, R.S. Kurmanov, J.S. Vaagen, and J.M. Bang, Phys. Rev. C **43**, 2835 (1991).
[15] S.N. Ershov, T. Rogde, B.V. Danilin, J.S. Vaagen, I.J. Thompson, and F.A. Gareev, Phys. Rev. C **56**, 1483 (1997).
[16] S.N. Ershov, B.V. Danilin, T. Rogde, and J.S. Vaagen, Phys. Rev. Lett. **82**, 908 (1999).

[17] S.N. Ershov, B.V. Danilin, and J.S. Vaagen, Phys. Rev. C **62**, 041001(R) (2000).
[18] L.V. Chulkov *et al.*, Phys. Rev. Lett. **79**, 201 (1997).
[19] D. Aleksandrov *et al.*, Nucl. Phys. **A633**, 234 (1998).
[20] D. Aleksandrov *et al.*, Nucl. Phys. **A669**, 51 (2000).
[21] N. Austern and C.M. Vincent, Phys. Rev. C **23**, 1847 (1981).
[22] T. Udagawa and T. Tamura, Phys. Rev. C **24**, 1348 (1981).
[23] A. Kasano and M. Ichimura, Phys. Lett. **115B**, 81 (1982).
[24] M. Ichimura, N. Austern, and C.M. Vincent, Phys. Rev. C **32**, 431 (1985).
[25] M.V. Zhukov, B.V. Danilin, D.V. Fedorov, J.M. Bang, I.J. Thompson, and J.S. Vaagen, Phys. Rep. **231**, 151 (1993).
[26] B.V. Danilin, M.V. Zhukov, A.A. Korsheninnikov, L.V. Chulkov, and V.D. Efros, Sov. J. Nucl. Phys. **49**, 217 (1989); **53**, 45 (1991).
[27] B.V. Danilin and M.V. Zhukov, Yad. Fiz. **56**, 67 1993 [Sov. J. Nucl. Phys. **56**, 460 (1993)].
[28] B.V. Danilin, T. Rogde, S.N. Ershov, H. Heiberg-Andersen, J.S. Vaagen, I.J. Thompson, and M.V. Zhukov, Phys. Rev. C **55**, R577 (1997).
[29] F.A. Gareev, S.N. Ershov, A.A. Ogloblin, and S.B. Sakuta, Fiz. Elem. Chastits At. Yadra **20**, 1293 (1989) [Sov. J. Part. Nucl. **20**, 541 (1989)].
[30] F. Petrovich, R.J. Philpott, A.W. Carpenter, and J.A. Carr, Nucl. Phys. **A425**, 609 (1984).
[31] J. Raynal and J. Revai, Nuovo Cimento A **68**, 612 (1970).
[32] J.H. Kelly *et al.*, Phys. Rev. Lett. **77**, 502 (1996).
[33] H. Esbensen and G.F. Bertsch, Nucl. Phys. **A600**, 37 (1996).
[34] F. Rybicki and N. Austern, Phys. Rev. C **6**, 1525 (1972).
[35] C.M. Vincent and H.T. Fortune, Phys. Rev. C **2**, 782 (1970).
[36] K. Alder, A. Bohr, T. Huus, B. Mottelson, and A. Winter, Rev. Mod. Phys. **28**, 432 (1956).
[37] J.S. McCarthy *et al.*, Phys. Rev. C **15**, 1396 (1977).
[38] M. El-Azab Farid and G.R. Satchler, Nucl. Phys. **A438**, 525 (1985).
[39] V.I. Kukulin *et al.*, Nucl. Phys. **A586**, 151 (1995).
[40] I.J. Thompson, B.V. Danilin, V.D. Efros, J.S. Vaagen, J.M. Bang, and M.V. Zhukov, Phys. Rev. C **61**, 024318 (2000).
[41] B. V. Danilin, S.N. Ershov, and J. S. Vaagen (unpublished).
[42] M.A. Franey and W.G. Love, Phys. Rev. C **31**, 488 (1985).
[43] J.Y. Hostachy *et al.*, Nucl. Phys. **A490**, 441 (1988).
[44] M.E. Brandan, Phys. Rev. Lett. **60**, 784 (1988).
[45] O.V. Bochkarev *et al.*, Yad. Fiz. **46**, 12 (1987) [Sov. J. Nucl. Phys. **46**, 7 (1987)].
[46] O.V. Bochkarev *et al.*, Yad. Fiz. **57**, 5 (1994) [Phys. At. Nucl. **57**, 1281 (1994)].
[47] M.V. Zhukov, L.V. Chulkov, B.V. Danilin, and A.A. Korsheninnikov, Nucl. Phys. **A553**, 428 (1991).